Acta Biomaterialia 213 (2026) 737–756

Contents lists available at ScienceDirect

Acta Biomaterialia

journal homepage: www.elsevier.com/locate/actbio

Full length article

Extrusion-based additive manufacturing of zinc bone scaffolds

Keyu Chen *, Jiahui Dong, Niko Eka Putra, Jinlai Li, Maria Klimopoulou, Marius A. Leeflang, Lidy Elena Fratila-Apachitei, Jie Zhou, Amir A. Zadpoor

Department of Biomechanical Engineering, Faculty of Mechanical Engineering, Delft University of Technology, Mekelweg 2, Delft 2628 CD, the Netherlands

ARTICLE INFO

Keywords:
Zinc
Material extrusion
Additive manufacturing
Bone implant
Biodegradation
Cytocompatibility

ABSTRACT

Zinc (Zn) has emerged as a promising biodegradable metal for bone tissue engineering, yet fabricating porous scaffolds via laser-based additive manufacturing (AM) remains challenging due to Zn evaporation. This study presents the successful fabrication of porous Zn scaffolds via extrusion-based AM through systematic ink formulation and sintering optimization. Printability was optimized through rheological analysis of 50–56 vol % Zn-loaded inks, while sintering conditions were refined within a precise temperature window. SEM and micro-CT characterized sintering quality and quantified pore defects. Optimal scaffolds, printed with 53 vol % ink and sintered at 415 °C for 5 h, achieved 40 ± 3% absolute porosity with minimal evaporation, attributed to a hybrid solid-liquid phase sintering mechanism. The scaffolds exhibited trabecular bone-matching mechanical properties with compressive yield strength of 16.1 ± 1.3 MPa and elastic modulus of 1.4 ± 0.1 GPa. *In vitro* biodegradation in r-SBF showed a corrosion rate of 0.03 ± 0.01 mm/year after 28 days, with biodegradation products including ZnO, $Ca_3(PO_4)_2$, and Zn-phosphate/chloride hydrates. Electrochemical tests demonstrated increasing polarization resistance (21.1 ± 3.8 kΩ·cm^2) and passivation behavior. Indirect cytocompatibility assays showed > 90% metabolic activity for MC3T3-E1 cells in ≤ 50% Zn extracts, while direct seeding confirmed cell adhesion. These results establish extrusion-based AM as a viable route for fabricating Zn scaffolds with tailored porosity, controlled biodegradation, bone-like properties, and acceptable cytocompatibility, advancing the development of Zn-based biodegradable implants.

Statement of significance: Although laser-based additive manufacturing of pure zinc and its alloys is becoming increasingly mature, its inherent drawbacks, such as evaporation-driven composition loss and melt-pool instabilities, remain non-negligible and underscore the need to develop and apply alternative AM strategies for Zn-based bone scaffolds. We presented an extrusion-based route to fabricate porous Zn bone scaffolds and establish an end-to-end workflow spanning ink formulation, debinding, sintering, and multi-scale characterization. By tailoring the binder system and defining a robust thermal window, we achieved high-fidelity architectures with densified struts. The resulting scaffolds displayed bone-mimicking mechanical behavior together with predictable *in-vitro* degradation and cytocompatibility. Our work positions extrusion-based 3D printing as a practical manufacturing platform for Zn-based biodegradable bone substitutes.

1. Introduction

Safe and functional bone-substituting biomaterials are sought after to treat critical-sized bone defects. This quest has been triggered by the severe shortage of natural bone grafts and the unmet demands of an aging population [1]. In recent years, in addition to ceramic and polymeric biomaterials, biodegradable metals have been intensively studied as temporary bone-substituting materials [2]. The following significant advantages have been demonstrated. (i) Compared to polymeric [3] and ceramic biomaterials [4], metallic biomaterials offer improved mechanical performance, ensuring functional stability and reducing fracture risk immediately after implantation. (ii) Compared to bioinert metal implants, such as titanium (Ti) and its alloys [5], tantalum (Ta) [6], and cobalt-chromium alloys (CoCr) [7], biodegradable materials such as Zn can facilitate further progress of the bone regeneration process while eliminating long-term inflammatory responses and the need for a second surgery [8]. Zinc (Zn) and its alloys stand out among biodegradable metals for bone applications because of their suitable rates of biodegradability, good biocompatibility, and osteogenic potential, and have been considered to be promising candidates for use in

* Corresponding author.
E-mail address: K.Chen-6@tudelft.nl (K. Chen).

https://doi.org/10.1016/j.actbio.2026.01.039
Received 4 September 2025; Received in revised form 18 January 2026; Accepted 20 January 2026
Available online 24 January 2026

the treatment of critical-sized bone defects [9].

To satisfy the requirements of an ideal bone substitute, Zn-based biomaterials need to have a bone-mimicking multi-scale porous structure with interconnected macro- and micro-pores to facilitate cell adhesion, tissue ingrowth as well as vascular remodeling [10]. They also require a geometry that matches that of the bony defect to achieve reliable fixation and optimal stress distribution [11]. Traditional implant manufacturing techniques, such as casting and forging, followed by machining, face significant challenges in producing scaffolds with complex macro-pore and micro-pore-integrated structures [12]. Conventional powder metallurgy (PM) combined with spark plasma sintering (SPS) [13] and hot pressing sintering (HPS) [14] has been reported to be capable of manufacturing porous Zn-based alloys [15]. However, these methods cannot produce interconnected porous structures and complex external geometries. Laser-based additive manufacturing (AM) technologies, such as laser powder bed fusion (LPBF) enable the fabrication of porous scaffolds with intricate structures and allow for customizing implants tailored to individual patients [16–18]. Although the research on the LPBF technology for processing Zn implants has made significant progress, it remains in its early stages [19–22]. Element loss and microporosity control are the two interconnected problems encountered in processing Zn *via* LPBF, mainly due to the severe evaporation of Zn during intense melting under high-energy laser [23]. Significant evaporation and smoke generation have a profound impact on the stability of the melt pool, leading to numerous defects, including pores, bubbles, microcracks, residual stress, and deformation in the 3D-printed parts. In the early work of Montani *et al.*, a relative density of only 88 % was achieved for Zn [24]. Although Demir et al. [25] achieved a relative density of 98 % by incorporating an auxiliary gas-jetting device into the LPBF system, modifying the existing LPBF system poses new challenges regarding process gas handling.

While the Young's modulus of pure Zn (97 GPa) [26] can be adjusted to match that of the natural bone (cortical bone: 5–23 GPa; trabecular bone: 0.01–1.6 GPa) [27] by regulating the implant's porosity, the yield strength of pure Zn is only 28 MPa (in the as-cast state), which is far from the strength requirement for load-bearing bone implants (> 200 MPa) [28]. In addition, Zn scaffolds have been reported to exhibit *in vitro* cytotoxicity due to excessive ion release [29,30]. To address these issues, strategies have been adopted to develop Zn-based implants by adding alloying elements (*e.g.*, Li, Mg, *Ca*, Sr, Cu, or Ag) [21,31] to Zn and by functional doping with ceramic biomaterials such as bioactive glass, hydroxyapatite (HA) and tri-calcium phosphate (TCP) [32,33], to enhance their mechanical properties and bioactivity [34]. Since different elements have different boiling points and, thus, different evaporation susceptibilities under high-energy lasers, the chemical compositions of many Zn alloys prepared by LPBF often deviate from the original powder compositions [35]. In addition, adding a second material will alter the powder's flowability, and laser reflectivity, which may cause printing failure [36]. Therefore, it is essential to develop a more straightforward, economical, and efficient processing technology for porous Zn alloy and composite implants that offers flexibility in structural and material design.

In recent years, extrusion-based AM technology [37,38], a two-step AM process based on ink extrusion, has proven effective for fabricating metallic scaffolds with complex structures. The first step of this process is to print a green part with ink composed of metal powder and binder. This is followed by the second step aimed at transforming the green part into a firmly bonded, robust scaffold through debinding and sintering [39,40]. This AM technology has prepared bio-inspired titanium alloy implants [41] and high-entropy alloy scaffolds [42]. It has also been successfully applied to create biodegradable magnesium- [43,44] and iron-based [45,46] implants, yielding fully interconnected, long-range, porous structures with varied pore sizes. In addition, extrusion-based AM allows for the addition of alloying elements (MgZn [39], FeMn [47]) and bioceramics (Mg-TCP [44], Fe-akermanite (Ak) [48], and FeMn-Ak [49]). Applying this AM technology to Zn will circumvent the problems associated with LPBF, such as melt-pool instability, Zn loss, defects, and high costs.

To this end, in this study, we made the first attempt to fabricate pure Zn scaffolds using extrusion-based AM. First, we developed an ink formulation by selecting a suitable binder system and optimizing the ink loaded with Zn powder. We also optimized the sintering conditions, aided by microstructural and micro-CT analyses. Subsequently, we characterized the 3D-printed Zn scaffolds in terms of *in vitro* degradation, electrochemical behavior, time-dependent mechanical properties, and cytocompatibility. In addition, herein we propose a unique Zn powder sintering mechanism based on our experimental observations and explain the mechanisms of Zn scaffold biodegradation *in vitro*.

2. Materials and methods

2.1. Scaffold design, 3D printing, and post-processing

A commercial nitrogen-atomized pure Zn powder (impurity <0.01 wt %, Nanoval GmbH, Germany) with a spherical shape (Fig. 1a) and *D*-values of 8.8 μm (D10), 23.6 μm (D50), and 45.4 μm (D90) (Fig. 1b) was employed as the raw material. Particle size distribution was provided by the powder manufacturer (Batch AZ/003/BVF-50 μm). A cylindrical scaffold with a diameter of 12.38 mm and a height of 12.64 mm was designed (Fig. 1c). The designed structure had the following characteristics: strut size = 580 μm, strut spacing = 360 μm, and layer number = 27. A 0 °/90 °/0 ° lay-down pattern was used for the scaffold, which was designed using custom software integrated with the 3D BioScaffolder printer (BS 3.2, GeSim, Germany). The scaffold was designed with a porosity of 37.8 %, a value selected to target the mechanical properties of human trabecular bone while maintaining sufficient pore space for potential bone ingrowth [50–52]. The steps involved in fabricating the scaffolds, including ink preparation, 3D printing, debinding, and sintering, are illustrated in Fig. 1d.

In step 1, inks loaded with the Zn powder were prepared by mixing the Zn powder with a binder system composed of polyvinylpyrrolidone polymer (PVP, $M_w \sim 40000$, Sigma Aldrich, Germany), 1-octanol (≥99 %, Sigma-Aldrich), and ethyl alcohol (Sigma-Aldrich). A series of trials were performed to determine the printability and debinding behavior of binders with different compositions. Inks with 50, 53, and 56 vol % Zn powder loading were then prepared for rheological characterization and subsequent optimization of the printing process. The rheological properties of the prepared inks were determined using a rheometer (Physica MCR 301, Anton Paar, Germany). In step 2, the ink was extruded to form the designed scaffold through a tapered nozzle with a tip diameter of 580 μm under an applied pressure of 160 kPa and at a printing speed of 10 mm/s. Step 3 included debinding and sintering under a controlled argon atmosphere, prior to which the dried Zn scaffolds were loaded into a tube furnace (STF16/180, Carbolite Gero Ltd., UK). To determine the debinding condition, thermogravimetric analysis (TGA) of PVP was performed using an SDT Q600 v20.9 thermogravimetric analyzer (TA Instruments, USA) to determine the exact temperature at which the binder evaporates. Based on the TGA analysis, the 3D-printed green samples were heated from room temperature to 350 °C at a heating rate of 2 °C/min, and a dwelling time of 1 h was provided for debinding. To determine the sintering conditions, a differential scanning calorimeter (DSC) (Discovery DSC250, TA Instruments, USA) was used to measure the actual melting point of the Zn powder at a heating and cooling rate of 10 °C/min over a temperature range of 20 to 500 °C. Based on the DSC analysis, the debonded samples were heated at a heating rate of 2 °C/min to perform sintering at different temperatures (*i.e.*, 412, 415, and 418 °C) and for various durations (*i.e.*, 3, 5, and 7 h) under a highly pure argon atmosphere (purity: 99.9999 %; inlet pressure: 1 bar). Afterward, the as-sintered Zn scaffolds were ultrasonically cleaned in isopropyl alcohol for 10 min before subsequent characterization.

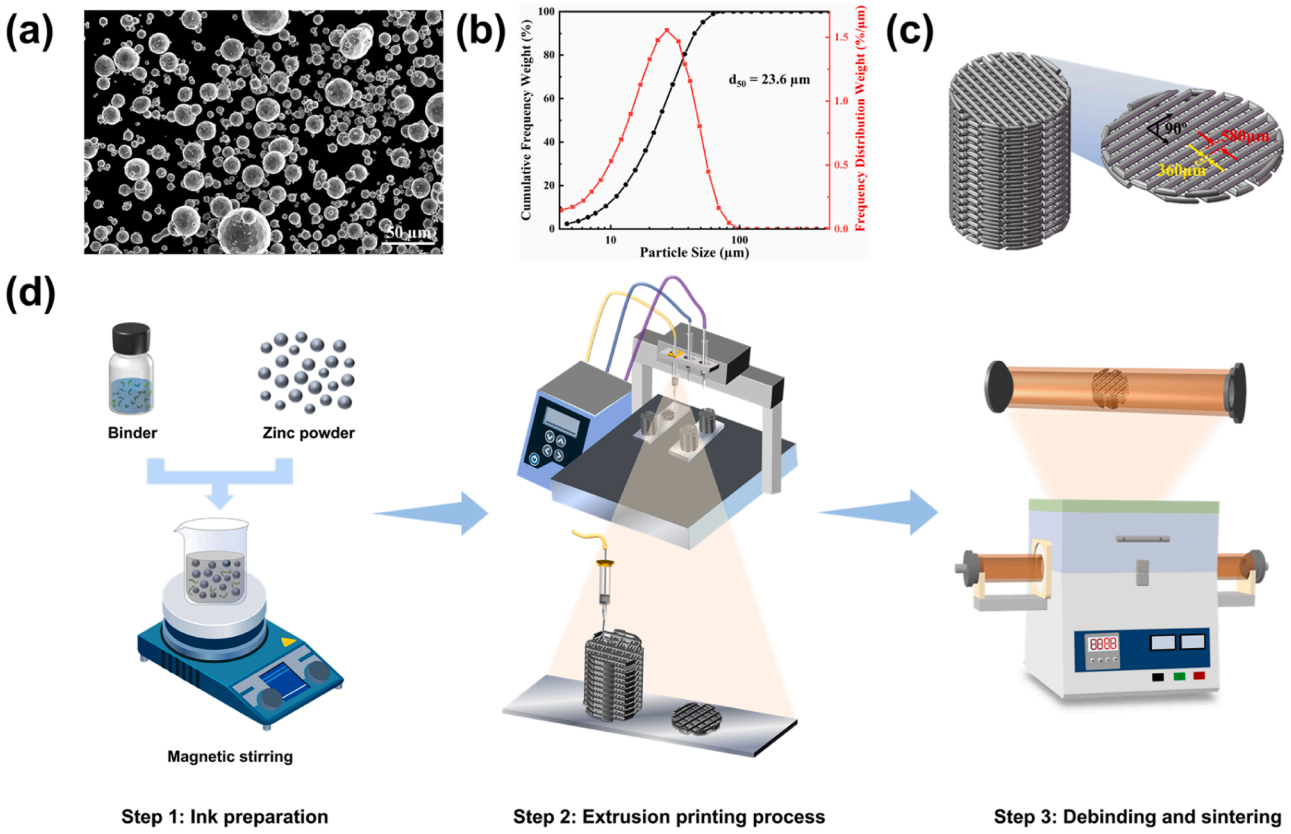

Fig. 1. (a) Morphology of the as-received pure Zn powder, (b) particle size distribution of the Zn powder, (c) CAD design of the Zn scaffold, and (d) schematic illustrations of the Zn scaffold fabrication steps *via* extrusion-based AM [2].

2.2. Structural characterization of the fabricated scaffolds

The morphology and strut integrity of the as-printed Zn scaffolds were examined using a scanning electron microscope (SEM, JSM-IT100, JEOL, Japan). The as-sintered Zn scaffolds' morphology and cross-section microstructure were observed using the SEM, equipped with an energy-dispersive X-ray spectroscope (EDS). The specimens were ground and polished to a mesh grade of 4000. The absolute porosity of the as-sintered Zn scaffolds was determined using the dry weighing method:

$$\varphi_s = \left(1 - \frac{m_s/\rho_{Zn}}{V_{bulk}}\right) \times 100\% \quad (1)$$

where φ_s is the absolute porosity of the as-sintered Zn scaffold [%], m_s is the mass of the as-sintered Zn scaffold [g], V_{bulk} is the bulk volume [cm^3], and ρ_{Zn} is the theoretical density of Zn (*i.e.*, 7.14 g/cm^3). The as-printed and as-sintered scaffolds (3, 5, and 7 h) were imaged by using X-ray micro-computed tomography (μCT, Nanotom 180NF, Phoenix) at a current of 140 μA, a voltage of 140 kV, and a voxel size of 10 μm. Sizes and distribution of pores in the as-printed and as-sintered Zn scaffolds were analyzed using the VG Studio Max software. To ensure the data's validity, only the pores with equivalent diameters exceeding 30 μm (*i.e.*, 3 times the voxel size [53]) were used in the analysis. The equivalent diameter [ϕ] and sphericity [ψ] were used to evaluate the size and shape of the pores [41]. Specifically, the equivalent diameter ϕ represents the diameter of a sphere that would have the same volume as the measured pore. Sphericity ψ is a measure of how closely the shape of the pore resembles a perfect sphere, where a value of 1.0 indicates a perfect sphere. These parameters were calculated as follows:

$$\phi = \sqrt[3]{6V/\pi} \quad (2)$$

$$\psi = \sqrt[3]{36\pi V^2}\Big/S \quad (3)$$

where V and S are the pore volume and surface area, respectively. Phase analysis was conducted using a Bruker D8 Advance X-ray diffractometer (XRD) (Cu *Ka* radiation) over a scanning range of 10 – 100 ° with a step size of 0.021 °.

2.3. Biodegradation experiments

In vitro immersion tests of the Zn scaffolds ($n = 4$) were performed in the revised simulated body fluid (r-SBF) [54] for up to 28 days in a thermal bath maintained at 37 ± 0.1 °C. All specimens used for the experiments described hereafter were prepared using the optimized sintering process (415°C for 5 h). The immersion ratio (*i.e.*, the ratio of solution volume to sample area) was 20 mL/cm^2. The total surface area of the specimens exposed to the r-SBF was 64.3 cm^2. Data analysis time points were selected as 1, 3, 7, 14, and 28 days. The pH values of the r-SBF were monitored throughout the immersion period using a pH electrode (InLab Expert Pro-ISM, METTLER TOLEDO, Switzerland). An inductively coupled plasma optical emission spectroscope (ICP-OES, iCAP 6500 Duo Thermo Fisher, USA) was used to measure the concentrations of Zn, *Ca*, and P ions in the r-SBF solution at the selected time points. A chemical cleaning solution (*i.e.*, 100 g /L NH_4Cl at 70 °C for 2 - 5 min, according to the ISO 8407 standard [55]) was used to remove the biodegradation products from the surface. The corrosion rate (CR_W, mm/y) of the Zn scaffolds was calculated from weight loss according to the ASTM G31–72 standard [56]:

$$CR_w = 8.76 \times 10^4 \times \frac{m}{A \times \rho \times t} \quad (4)$$

where m is the mass loss [g], A is the surface area of the scaffold [cm^2] based on the initial scaffold design value, ρ is the theoretical density of pure Zn (*i.e.*, 7.14 g/cm^3), and t is the duration of *in vitro* immersion [h]. Fourier-transform infrared spectroscopy (FTIR) (Thermo-Nicolet Nexus, USA) and X-ray photoelectron spectroscopy (XPS, Thermo Fisher Scientific, K-Alpha Model, USA) were used to characterize the surface chemical states of the Zn scaffolds before and after the *in vitro* immersion experiments.

2.4. Electrochemical tests

The electrochemical response of the Zn scaffold specimens ($n = 3$) in the r-SBF at 37 ± 0.5 °C was studied using a Bio-Logic SP-200 potentiostat (Bio-Logic Science Instruments, France). All specimens used for the experiments described hereafter were prepared using the optimized sintering process (415 °C for 5 h). A three-electrode electrochemical cell was set up with graphite as the counter electrode, Ag/AgCl as the reference electrode, and Zn scaffold sample as the working electrode. To prepare the working electrodes, the Zn specimens were connected to a copper wire using copper foil tape and were then mounted into epoxy resin. The samples were carefully embedded so that only the top, flat circular surface was left exposed to the r-SBF solution, while all other surfaces were sealed. The surface area of the specimens exposed to the electrolyte was 0.58 cm^2. Before the electrochemical tests, the setup was allowed to reach a stable open circuit potential (OCP) for 1 h. The linear polarization resistance (LPR) tests were carried out from −25 to +25 mV *versus* OCP at a scan rate of 0.167 mV/s. The electrochemical impedance spectroscopy (EIS) tests were conducted using a sine amplitude of 10 mV *versus* OCP over a frequency scan between 200 kHz to 10 mHz. The impedance data were analyzed using the EC-Lab software (Bio-LogicScience Instruments, Claix, France). In addition, potentiodynamic polarization (PDP) tests were performed with polarization between −300 and +500 mV *versus* OCP at a scan rate of 0.5 mV/s. From the PDP results, corrosion rates (CR_E, mm/y) were calculated according to the ASTM G102–89 standard [57]:

$$CR_E = 3.27 \times 10^{-3} \times EW \times \frac{i_{corr}}{\rho} \quad (5)$$

where EW is the equivalent weight of Zn (valence 2), i_{corr} is the current density [μA/cm^2], and ρ is the theoretical density of pure Zn [g/cm^3].

2.5. Mechanical tests

Uniaxial compression tests of the as-fabricated Zn scaffold specimens ($n = 4$), as well as the Zn scaffold specimens retrieved after 1, 3, 7, 14, and 28 days of *in vitro* immersion, were performed using an Instron universal mechanical testing machine (ElectroPuls E10000, Germany) with a 10 kN load cell at a crosshead speed of 2 mm/min. The uniaxial compression tests were conducted specifically along the building direction (*i.e.*, the Z-axis). The yield strengths and elastic moduli of the porous Zn specimens before and after the *in vitro* immersion tests were determined according to the ISO 13314:2011 standard [49].

2.6. Cytocompatibility evaluation

2.6.1. Preculture of cells and preparation of extracts

Preosteoblast cells MC3T3-E1 (Sigma Aldrich, Germany) were precultured for 7 days in α-minimum essential medium (α-MEM, Thermo Fisher Scientific, USA) supplemented with 10 % fetal bovine serum (FBS, Thermo Fisher Scientific, USA) and 1 % penicillin/streptomycin (p/s, Thermo Fisher Scientific, USA) under 5 % CO_2 and at 37 °C. The medium was refreshed every 2–3 days. Following the preculture, the cells were harvested, counted, and seeded for the follow-up experiments. From day 2, the cells were supplied with osteogenic medium containing 50 μg mL^{-1} ascorbic acid (1:1000) and 4 mM β-glycerophosphate (1:500) (both from Sigma Aldrich, Germany). The Zn scaffolds were heated in an oven at 120 °C for 2 h for sterilization. Extracts from the sterilized Zn scaffolds were prepared by immersing them in α-MEM at a specimen-to-medium ratio of 1.25 cm^2/mL [58] for 72 h under the same condition. The resulting supernatants were collected, filtered, and diluted with α-MEM to obtain 75 %, 50 %, 25 %, and 10 % extracts.

2.6.2. Indirect cytotoxicity tests

PrestoBlue assay (Thermo Fisher Scientific, USA) was used to evaluate the cytotoxicity of the Zn scaffolds extracts. Firstly, 5×10^3 MC3T3-E1 preosteoblast cells were cultured in 300 μL of α-MEM (with 10 % FBS and 1 % p/s) in 48 well plate for 24 h, prior to exchanging the α-MEM with the Zn scaffold extracts ($n = 3$). The same number of cells was cultured in the original α-MEM, as the negative control. After 1, 3, and 7 days of culture, the zinc extract media were replaced with 270 μL fresh pure α-MEM to prevent the interference of zinc ions with the assay. Consecutively, 30 μL of PrestoBlue reagents (Thermo Fisher Scientific, USA) were added, and the specimens were incubated at 37 °C for 1 h. The absorbance values were then measured using a Victor X3 microplate reader (Perkin Elmer, The Netherlands) over a 530 - 590 nm wavelength range. The average metabolic activity of the cells was calculated according to the following equation:

$$Metabolic\ activity\ [\%] = \frac{Absorbance\ (specimen)}{Absorbance\ (negative\ control)} \times 100 \quad (6)$$

To observe the morphology of the cells grown in the extracts, MC3T3-E1 cells (5×10^3) were cultured in 48-well plates with 300 μL extracts ($n = 3$). After 7 days of cell culture, the specimens were washed with phosphate-buffered saline (PBS, Sigma-Aldrich, Germany) and fixed using 4 % formaldehyde/PBS (Sigma-Aldrich, Germany) at room temperature for 15 min. Afterward, the cells were stained with rhodamine phalloidin (Thermo Fisher Scientific, USA) to label the cellular actin filaments and with 4′,6-diamidino-2-phenylindole (DAPI) (Thermo Fisher Scientific, USA) to label the cell nuclei. The specimens were observed and analyzed under a fluorescence microscope (ZOE Fluorescent Cell Imager, Bio-Rad, USA).

2.6.3. Direct cytotoxicity tests

A Trypan blue cell counting assay was performed to assess the cytocompatibility of the Zn scaffolds. The Zn scaffolds (2.4 mm in height and 9.3 mm in diameter, n=3) were pre-cultured with 300 μL α-MEM and 5×10^4 MC3T3-E1 cells in a 48-well plate. After 4 h of incubation, the scaffolds were transferred to a 6-well plate with 8 mL of α-MEM per well, attaining a specimen-to-medium ratio of 1.25 cm^2/mL. After 1, 3, and 7 days of culturing, the cells were trypsinized from the scaffolds and the well plates and then suspended. 10 μL of each cell suspension was mixed with 10 μL of trypan blue dye (Bio-Rad, USA) and subsequently pipetted into a dual-chamber cell counting slide. Live cell numbers were counted using an automated cell counter (TC20, Bio-Rad, USA). In addition, after 3 days of culture, 2 μL/mL of calcein (Thermo Fisher Scientific, USA) and 1.5 μL/mL of ethidium homodimer-1 (Thermo Fisher Scientific, USA) were used to stain the live and dead cells on the Zn scaffolds in the dark, at room temperature for 30 min. The specimens were then observed using a fluorescence microscope (ZOE Fluorescent Cell Imager, Bio-Rad, USA). For observing the morphologies of the cells under SEM, the specimens (n=2) were washed in PBS, fixated with 4 % formaldehyde (Sigma Aldrich, Germany) for 20 min, followed by dehydration in 30, 50, 70, and 100 % ethanol for 10 min each, and dried for 2 h.

2.7. Statistical analysis

All values are expressed as mean ± standard deviation. Statistical analysis of the results obtained from the PrestoBlue assay was performed with two-way ANOVA, followed by the Tukey *post hoc* test. For the cell count results obtained from the direct cultures, as well as the

compressive yield strength and modulus of the porous Zn specimens before and after the *in vitro* immersion, statistical analysis was conducted with one-way ANOVA, followed by the Tukey *post hoc* test (α= 0.05) with $p < 0.0001$, ****; $p < 0.001$, ***; $p < 0.01$ and **; $p < 0.05$, *. The statistical analysis of absolute porosity values and the maximum pore diameters was also conducted using one-way ANOVA, followed by the Tukey *post hoc* test. A *p*-value of less than 0.05 was considered statistically significant.

3. Results

3.1. Ink formulation and printing process optimization

The viscosity-shear stress/rate curves of the three inks with 50, 53, and 56 vol % Zn powder loading all showed a decline as the shear stress/rate increased (Fig. 2a and 2b), exhibiting the typical shear-thinning behavior. Under higher shear stresses (>500 Pa) and shear rates (>1 s^{-1}), the viscosity of the 50 vol % ink was lower than that of the other inks, suggesting that the ink with a lower percentage of Zn powder would be more prone to structural breakdown and would increase its flowability under high shear conditions. The frequency sweeping test showed that both the storage (G') and loss moduli (G'') increased with frequency (Fig. 2c). The increased G' indicated that all the as-prepared inks possessed a strong energy storage capacity, especially in the high-frequency range. For all three inks, the G' values were higher than the G'' values, suggesting elastic or solid-like behavior [40] across the frequency range. This characteristic is essential for maintaining the shape and rigidity of extruded structures and supporting the layers above.

The samples printed with the ink containing 50 vol % Zn powder exhibited large-scale collapse of almost all struts (Fig. 2d), making it challenging to maintain structural integrity and provide adequate support for the layers above. The samples printed with the inks containing 53 and 56 vol % Zn powder, however, maintained the structural integrity of the struts, thereby ensuring the shape fidelity of the scaffolds (Fig. 2e and f). This suggests that sufficient powder loading and strong bonding between powder particles and the binder are important factors in constructing scaffolds with a high aspect ratio, ensuring that they remain intact without obvious deformation or excessive shrinkage. Nevertheless, large cavities formed within the struts of the specimens printed with the ink containing 56 vol % Zn powder due to low fluidity (inset of Fig. 2f), which was expected to adversely affect the mechanical properties of the scaffold due to a decrease in the effective load-bearing cross-sectional area and the presence of stress concentration sites.

3.2. Sintering process optimization

According to the DSC and TGA results (Fig. 3a and b), the actual melting point of the Zn powder and the temperature at which PVP experienced the majority of its decomposition were measured to be 418.4 and 356.8 °C, respectively. Based on the results obtained from the ink formulation and printing process optimization presented in the preceding section, the ink with 53 vol % Zn powder was chosen to define the sintering process window (Fig. 3c). The experimental design involved a 3×3 matrix consisting of nine combinations (denoted as groups ① to ⑨) of sintering temperatures (412, 415, and 418 °C) and sintering times (3, 5, and 7 h). When sintering temperatures were set at 412 and 418 °C, insufficient sintering and overheating of the Zn powder were observed, regardless of sintering time. Due to inadequate sintering or poor bonding between powder particles, the scaffolds became prone to collapse and failure. The specimens maintained an effective porous structure when the sintering temperature was set to 415 °C. However, no significant macroscopic differences were observed between the specimens sintered for different durations. Further process optimization was performed to investigate the effects of sintering time on the sintering result of the Zn green part.

Fig. 3d depicts the further optimization of sintering time with the sintering temperature kept at 415 °C. SEM results confirmed high structural fidelity of the Zn scaffolds sintered for all three sintering durations (3, 5, and 7 h) (Figs. 4a, S1a, and S1c). At higher magnifications (Figs. 4b, S1b, and S1d), adequate bonding between Zn particles could be observed on the surface of the struts without noticeable pores and cavities caused by underdeveloped sintering necks and re-solidification. According to the XRD analysis (Fig. 4c), after sintering for 5 h, the specimens contained only two phases: Zn and ZnO, with no detectable

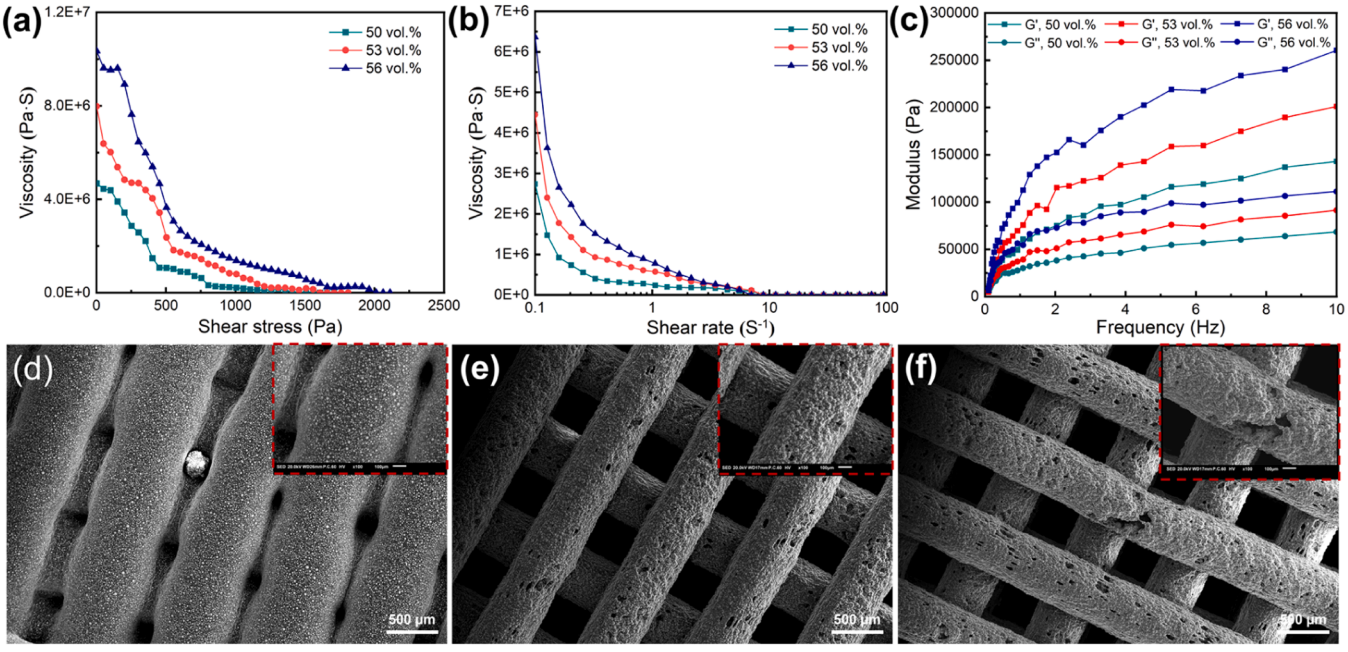

Fig. 2. The rheological characteristics of the Zn powder loaded inks and the corresponding printing quality: (a) the results of the shear stress sweep tests with applied stresses ranging between 1 and 2000 Pa, (b) the results of the shear rate sweep tests with shear rate ramping from 0.1 to 100 s^{-1}, (c) the G' and G'' values determined from the frequency-sweep tests, and (d, e, and f) the representative images of the scaffold struts printed from 50, 53, and 56 vol % Zn powder loaded inks, respectively. The insets show the high-magnification morphology and fidelity of individual struts, corresponding to the SEM images of Fig. 2d, e, and f.

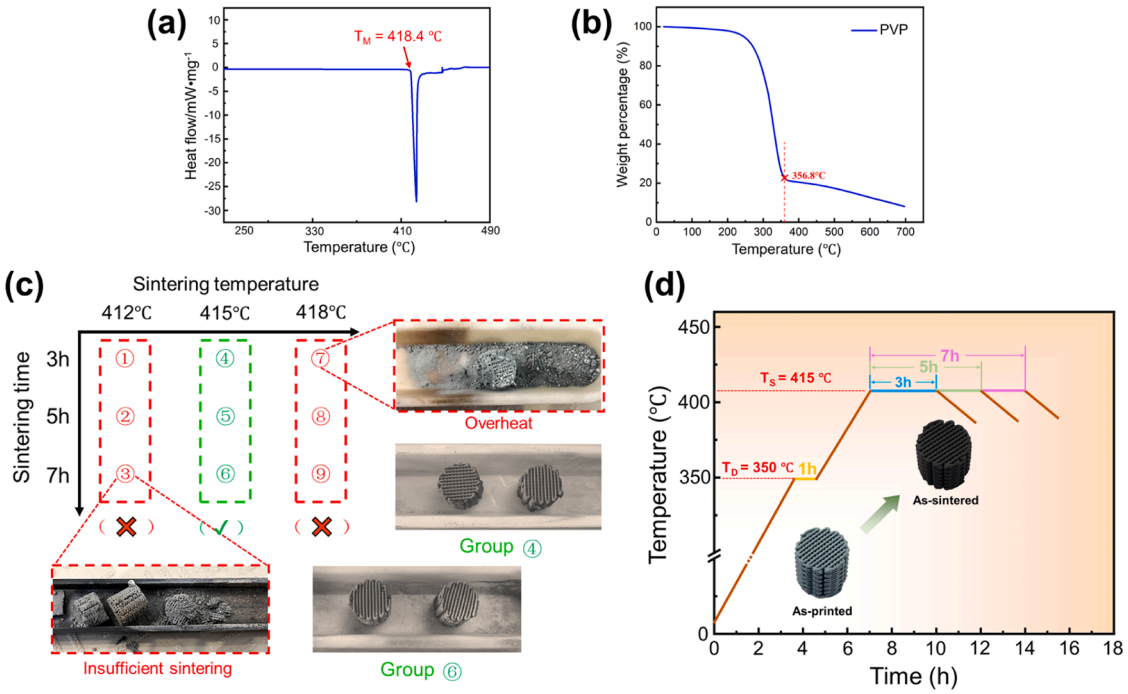

Fig. 3. The optimization of the sintering process for the Zn scaffolds: (a) the DSC curve of the pure Zn powder, (b) the TGA curve of the PVP powder, (c) the sintering optimization window, illustrating the effects of sintering temperature and sintering time on the quality of the sintered Zn scaffolds, and (d) an illustration of sintering process optimization with varied sintering times of 3, 5, and 7 h at a fixed sintering temperature of 415 °C.

binder residue. On the cross-section of the struts in the specimens sintered for 3 h, obvious pore defects were observed due to insufficient fusion of Zn powder particles (Fig. 4d and 4g). However, the number of such pore defects was significantly reduced when the sintering time was extended to 5 or 7 h, suggesting improved Zn particle fusion (Fig. 4e and 4f). However, after sintering for 7 h, a large number of nodules were observed on the surface of the Zn struts due to excessive flow of molten Zn and poor wettability of the molten Zn on solid Zn powder particles (Fig. 4f). Under this sintering condition, Zn particles on the periphery of the struts also experienced severe evaporation, leaving cavities and dimple-like features behind (Figs. 4i and S1d). After being subjected to external forces during grinding and polishing, the struts of the sample sintered for 3 h exhibited a loose and uneven surface (Fig. 4g). In contrast, the surfaces of the struts in the specimens sintered for 5 and 7 h were much denser. Still, the 7 h sintered sample showed some surface damage due to Zn evaporation and nodule formation (Fig. 4i). Overall, the 5 h sintering time was proven to be the optimum, considering both sintering defects and strut surface quality.

The three-dimensional reconstruction of the as-printed Zn scaffold and the scaffolds sintered for 3, 5, and 7 h using micro-CT confirmed that the chosen ink had good printability and that the printed Zn porous scaffolds had good sinterability without structural fracture or interlayer delamination (Fig. 5a). Pores as a printing defect (marked by the red arrows in Fig. 5a) caused by insufficient powder particle filling, and pores as a sintering defect (marked by the red dotted circles) were found inside the struts. Compared with the design values, the overall diameter and height of the cylindrical porous scaffolds in the as-printed state and as-sintered state were reduced, and the linear shrinkage increased with sintering time (Fig. 5b). Fig. 5c shows that the linear shrinkage of the struts increased with sintering time. Fig. 5d and Table 1 compares the absolute porosities of the scaffolds sintered for different durations, calculated using the weighing method and measured by micro-CT. The absolute porosity values of the as-printed Zn scaffold and the scaffolds sintered for 3, 5, and 7 h according to the weighing method were 35 ± 3, 38 ± 3, 40 ± 3 and 43 ± 2 %, respectively, while the values obtained from micro-CT analysis were 31 ± 2, 39 ± 3, 40 ± 3 and 43 ± 3 %, respectively. The absolute porosity values of the specimens sintered for 3 and 5 h were the closest to the designed value of 37.8 %.

Micro-CT analysis showed that compared with the as-printed state (Fig. 6a), the pore numbers in the as-sintered samples were significantly reduced (Fig. 6b–d). The analysis of the number of pores, presented in Fig. 6f–h, revealed that after sintering for 5 and 7 h, there were fewer pores than in the samples sintered for 3 h. The statistical distributions of the equivalent diameter and corresponding sphericity showed that the ψ values of all pores were less than 0.5, indicating that the pores were non-spherical printing defect pores rather than round gas holes, typically found in cast structures. From Table 1, the maximum ϕ values of the as-printed and sintered scaffolds (3, 5, and 7 h) were 381 ± 7, 363 ± 2, 337 ± 5, and 237 ± 4 mm, respectively, which indicated that the sintering times of 3 and 5 h helped reduce the small-sized printing pore defects. Still, a longer time (*i.e.*, 7 h) was required to allow for more effective Zn particle fusion, aided by liquid Zn, to eliminate the large-sized printing defect pores.

3.3. *In vitro* biodegradation behavior

After 28 days of static *in vitro* immersion in the r-SBF, white biodegradation products were deposited on the surface of the Zn struts and gradually filled the pores of the scaffolds (Fig. 7a). During the 28-day immersion period, the Zn scaffolds maintained their structural integrity without noticeable damage or collapse. The samples immersed for 28 days showed the highest accumulation of biodegradation products. XRD determined the biodegradation products to be ZnO, $Ca_3(PO_4)_2$, $Zn_3(PO_4)_2{\bullet}4H_2O$ and $Zn_5(OH)_8Cl_2{\bullet}H_2O$ (Fig. 7b). The concentration of released Zn^{2+} remained below 0.3 ppm throughout the 28 days of immersion. It had a rapid increase to 0.22 ppm in the first three days, then gradually decreased to 0.18 ppm by the 14th day, and finally increased to 0.27 ppm by the 28th day (Fig. 7c). The concentrations of

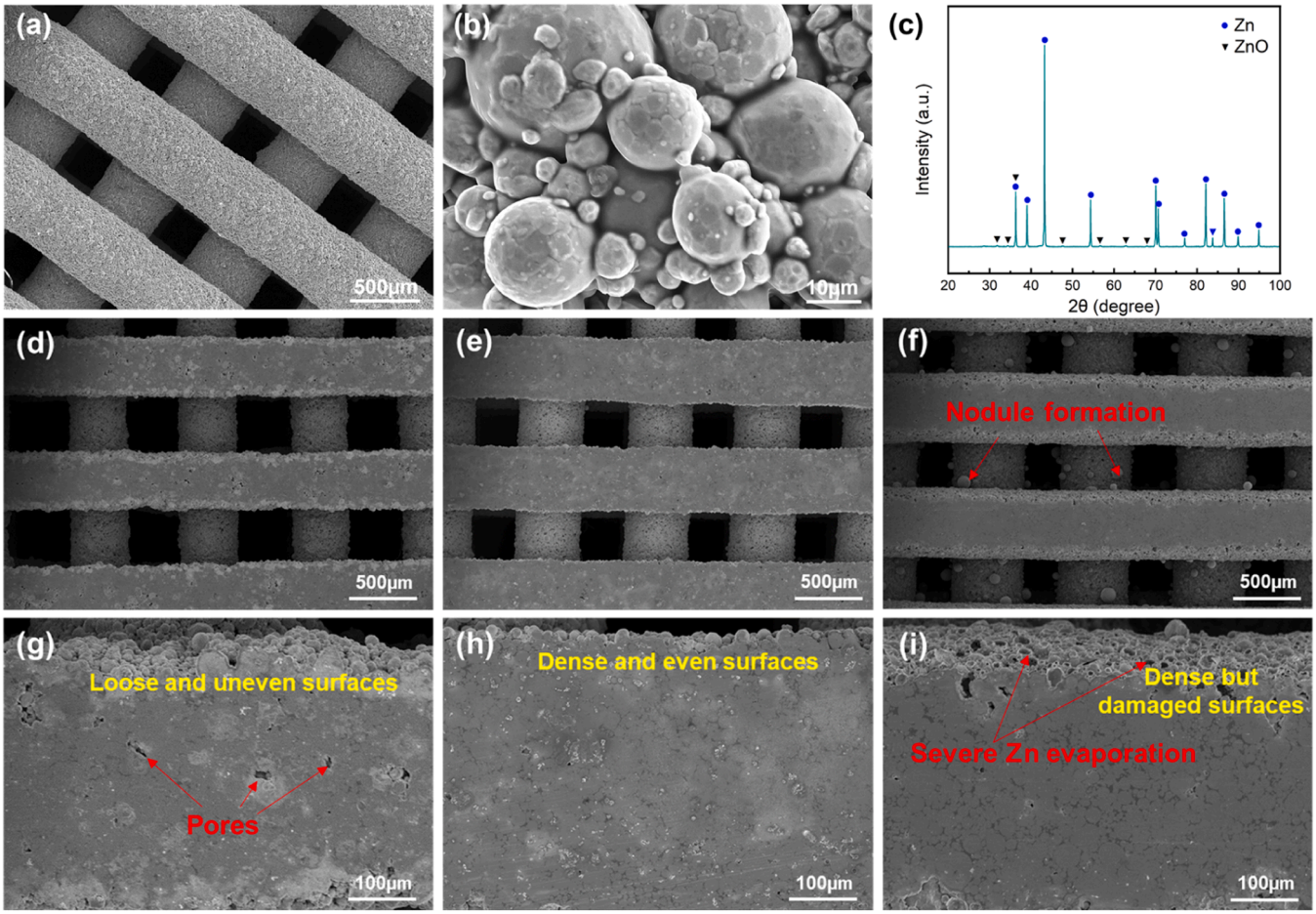

Fig. 4. Morphology, phase composition, and microstructures of the as-sintered Zn scaffolds sintered at 415 °C: (a) the representative strut morphology of the Zn scaffolds after sintering for 5 h, (b) the representative high-magnification view of the strut morphology, illustrating the particle bonding status in the Zn scaffold sintered for 5 h, (c) the XRD pattern of the Zn scaffold after sintering for 5 h, (d, e, and f) the representative cross-section images of the Zn scaffolds after sintering for 3, 5, and 7 h, respectively, and (g, h, and i) the corresponding high-magnification images of (d), (e) and (f), respectively, showing the sintering state of individual struts including surface morphologies and pore defects.

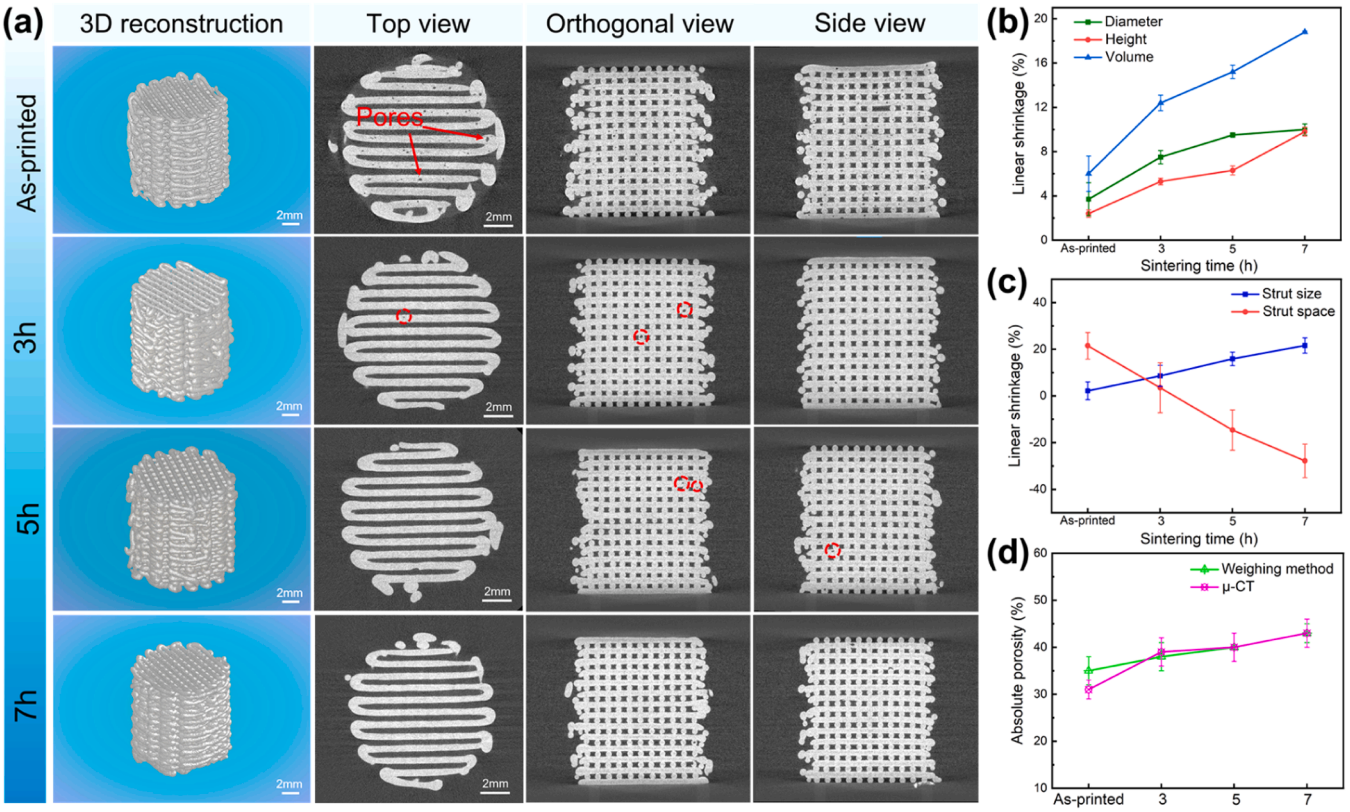

Fig. 5. The printability of the ink and sinterability of the as-printed Zn scaffold: (a) micro-CT reconstruction images, (b and c) linear shrinkages of the as-fabricated Zn scaffold as a whole and the corresponding struts as a function of sintering time, respectively, and (d) changes of the absolute porosity of the as-fabricated Zn scaffolds with sintering time.

Table 1
The morphological characteristics of the extrusion-based 3D-printed pure Zn scaffolds sintered for different times (n = 3; the weighing method and μCT analysis were used for the measurement of absolute porosity; the maximum pore diameter of printed and sintered Zn scaffolds were obtained through micro-CT scanning and 3D reconstruction).

Sintering time (h)	0 (As-printed)	3	5	7
Absolute porosity (Weighing, %)	35 ± 3^{a}	$38 \pm 3^{a,b}$	$40 \pm 3^{a,b}$	43 ± 2^{b}
Absolute porosity (μCT, %)	31 ± 2^{a}	$39 \pm 3^{a,b}$	40 ± 3^{b}	43 ± 3^{b}
Maximum pore diameter (ϕ, mm)	381 ± 7^{a}	363 ± 2^{b}	337 ± 5^{c}	237 ± 4^{d}

a–d: different superscript lowercase letters represent statistically significant differences between the groups of the pure Zn scaffolds with different sintering times at $p < 0.05$ (comparison within the same row).
The identical superscript lowercase letters indicate that the values are statistically not significantly different.

*Ca*and P ions in the r-SBF solution showed similar trends over time, both increasing slightly and then decreasing continuously (Fig. 7d). As the ion concentrations of the solution changed, the pH value increased to 8.0 ± 0.1 by the 28th day (Fig. 7e). The mass loss of the Zn scaffolds increased from 0.3 ± 0.1 % after 1 day of immersion to 3.6 ± 0.3 % after 28 days of immersion (Fig. 7f). The corrosion rates CR_W were calculated to be 0.06 ± 0.01 mm/year at 1 day and 0.03 ± 0.01 mm/year at 28 days (Fig. 7g). From FTIR (Fig. 8a), the characteristic peak bands at 3300 – 3700 cm^{-1} and the peak around 1600 cm^{-1} corresponded to OH^{-}. The spectral peaks of PO_4^{3-} were present at around 980 and 1150 cm^{-1}. The total XPS spectrum (Fig. 8b) showed that the biodegradation products consisted of Zn, O, C, P, *Ca*, Na, N, and S. The percentages of *Ca* and P increased with immersion time, while the percentage of Zn decreased. Furthermore, the high-resolution XPS spectra for Zn2p3/2, and P2p were collected from the sample surfaces after 14 and 28 days of *in vitro* biodegradation and then fitted (Fig. 8c–f). The peaks located at 1023, 1022.2, and 1021.8 eV might have originated from $Zn_3(PO_4)_2{\bullet}4H_2O$, ZnO, and $Zn_5(OH)_8Cl_2{\bullet}H_2O$ [59–61], respectively (Fig. 8c and 8d). The P2p peaks observed at 133 and 134 eV were likely due to $Ca_3(PO_4)_2$ and $Zn_3(PO_4)_2{\bullet}4H_2O$ [60], respectively (Fig. 8e and 8f).

After one day of *in vitro* immersion, the Zn scaffolds' surface morphologies remained unchanged with few biodegradation products accumulated (Fig. 9). However, after 3 and 7 days of *in vitro* immersion, the biodegradation products showed a fine granular morphology, with a sparse yet uniform distribution across the center and edge regions of the scaffold surface. The biodegradation products mainly contained Zn, C, O, *Ca*, P and Cl, as well as a small amount of S or Na. After 14 days of immersion, the morphology of the biodegradation products differed significantly between the center and the edge regions. In the center, large amounts of white biodegradation products were deposited and aggregated into clusters. In contrast, in the edge region, the biodegradation products showed a coarse granular morphology with distinct corrosion pits surrounding them. After 28 days, the biodegradation products in the central region exhibited a morphology consisting of numerous fine particles mixed with a few coarse particles. In contrast, the edge region displayed thick, fish-scale-like deposits covering the gaps and surfaces of the struts. EDS analysis of the cross-sections of the

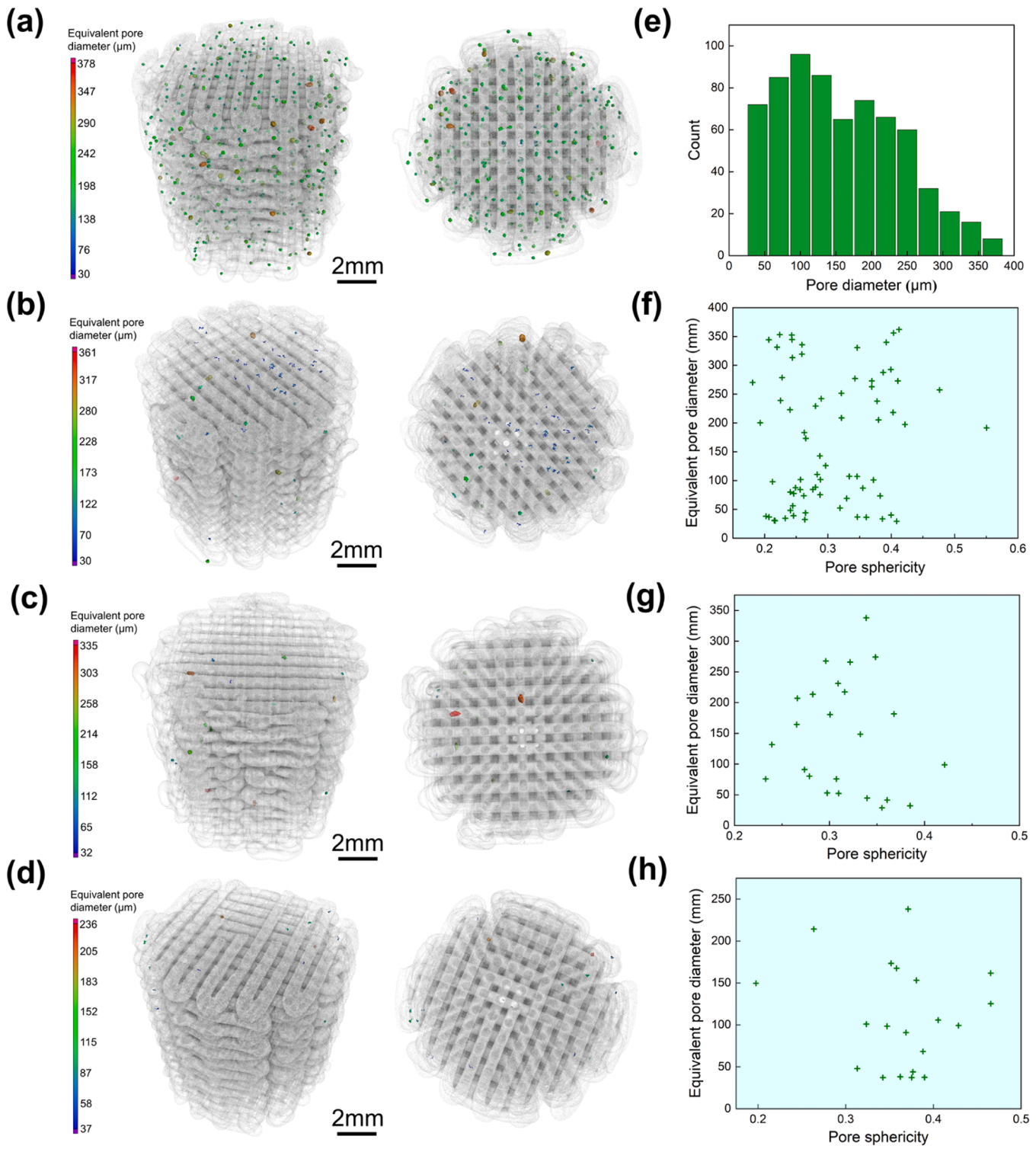

Fig. 6. (a–d) Micro-CT reconstruction images of the pore defects of the as-printed Zn scaffolds and the as-sintered scaffolds after 3, 5, and 7 h of sintering, respectively, and (e–h) qualitative analysis of pore sizes and numbers corresponding to (a), (b), (c) and (d), respectively.

struts in both the center and edge regions confirmed that the struts had undergone a certain degree of biodegradation.

3.4. Electrochemical measurements

As the corrosion time increased, the *OCP* value of the Zn scaffold increased from -946 ± 39 mV on day 1 to -805 ± 27 mV on day 28 (Fig. 10a). Meanwhile, the average R_p value decreased from 12.0 ± 2.9 kΩ.cm^2 on day 1 to a minimum of 7.4 ± 1.3 kΩ.cm^2 on day 7. Then, the average polarization resistance value gradually increased, reaching a peak of 21.1± 3.8 kΩ.cm^2 on the 28th day. According to the PDP curve (Fig. S2), the corrosion potential of the Zn scaffold changed from -925 ± 12 mV after 1 day to -874 ± 17 mV after 28 days. The corresponding corrosion current density decreased from 4.0 ± 0.2 μA/cm^2 to 2.5 ± 0.1 μA/cm^2. The corrosion rates CR_E calculated based on the current density were 0.059 and 0.038 mm/y after 1 day and 28 days of testing,

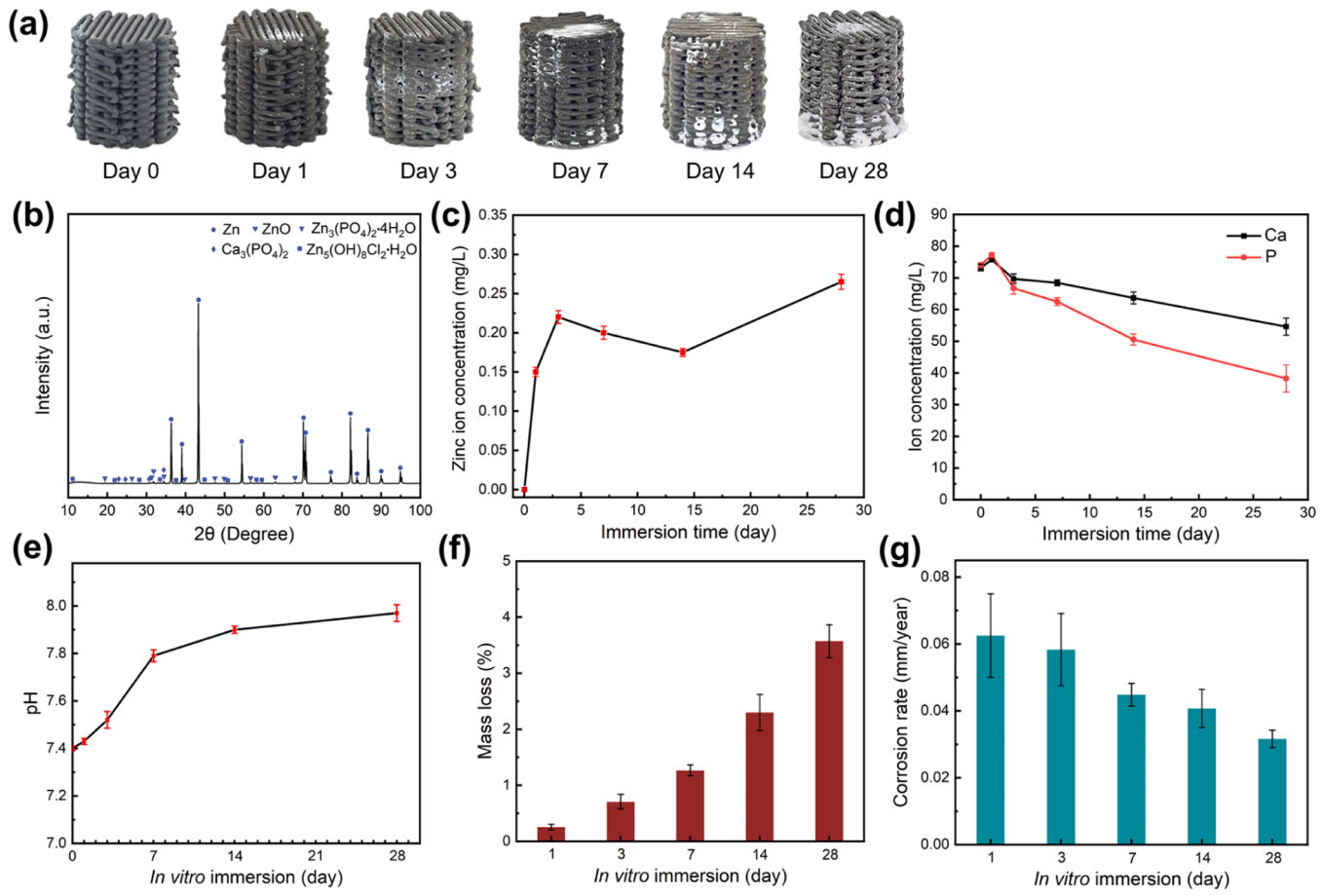

Fig. 7. *In vitro* degradation characteristics of the Zn scaffolds: (a) the optical macrographs of the biodegraded Zn specimens at different immersion time points, (b) XRD pattern of the biodegradation products on the Zn scaffolds at day 28, (c, d) the Zn, Ca, and P ion concentrations in the r-SBF throughout the immersion period, (e) pH variation up to 28 days of immersion, (f) the mass loss percentages, and (g) the corrosion rates of the scaffolds.

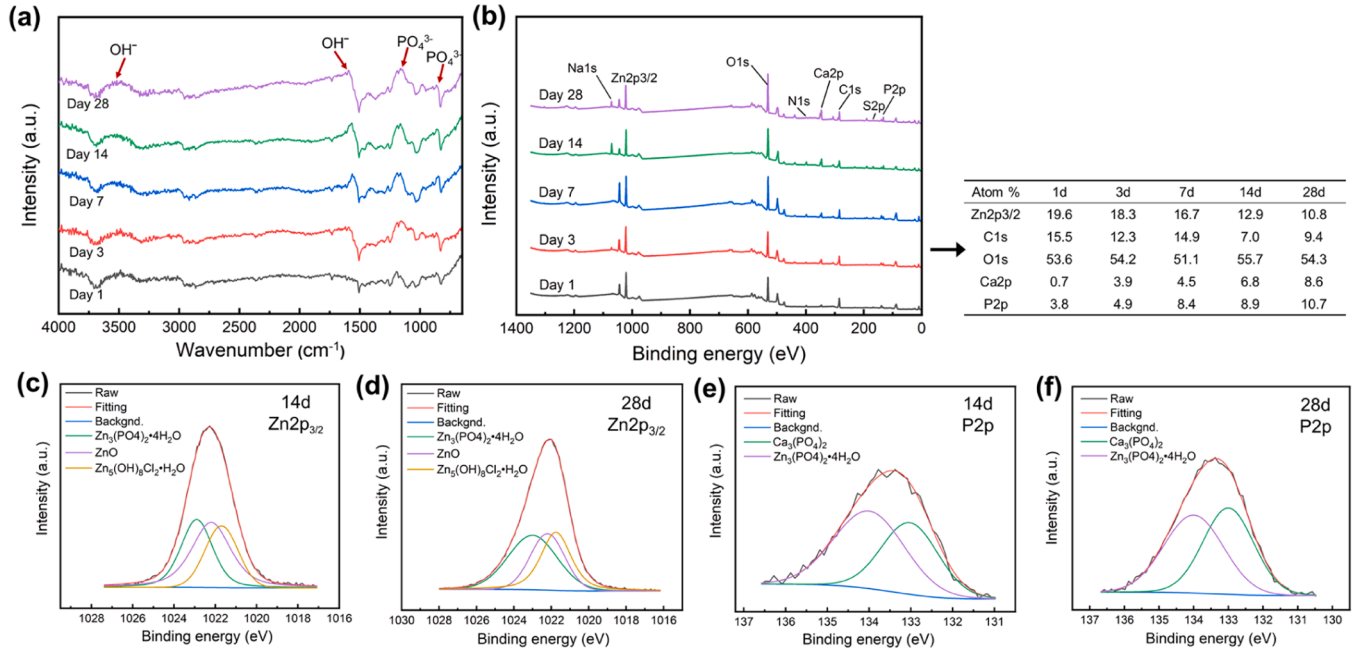

Atom %	1d	3d	7d	14d	28d
Zn2p3/2	19.6	18.3	16.7	12.9	10.8
C1s	15.5	12.3	14.9	7.0	9.4
O1s	53.6	54.2	51.1	55.7	54.3
Ca2p	0.7	3.9	4.5	6.8	8.6
P2p	3.8	4.9	8.4	8.9	10.7

Fig. 8. Composition analysis of the biodegradation products formed on the Zn scaffolds after *in vitro* immersion: (a) the FTIR spectrum, (b) XPS spectra, and (c-f) XPS deconvoluted spectra for $Zn2p_{3/2}$ and P2p.

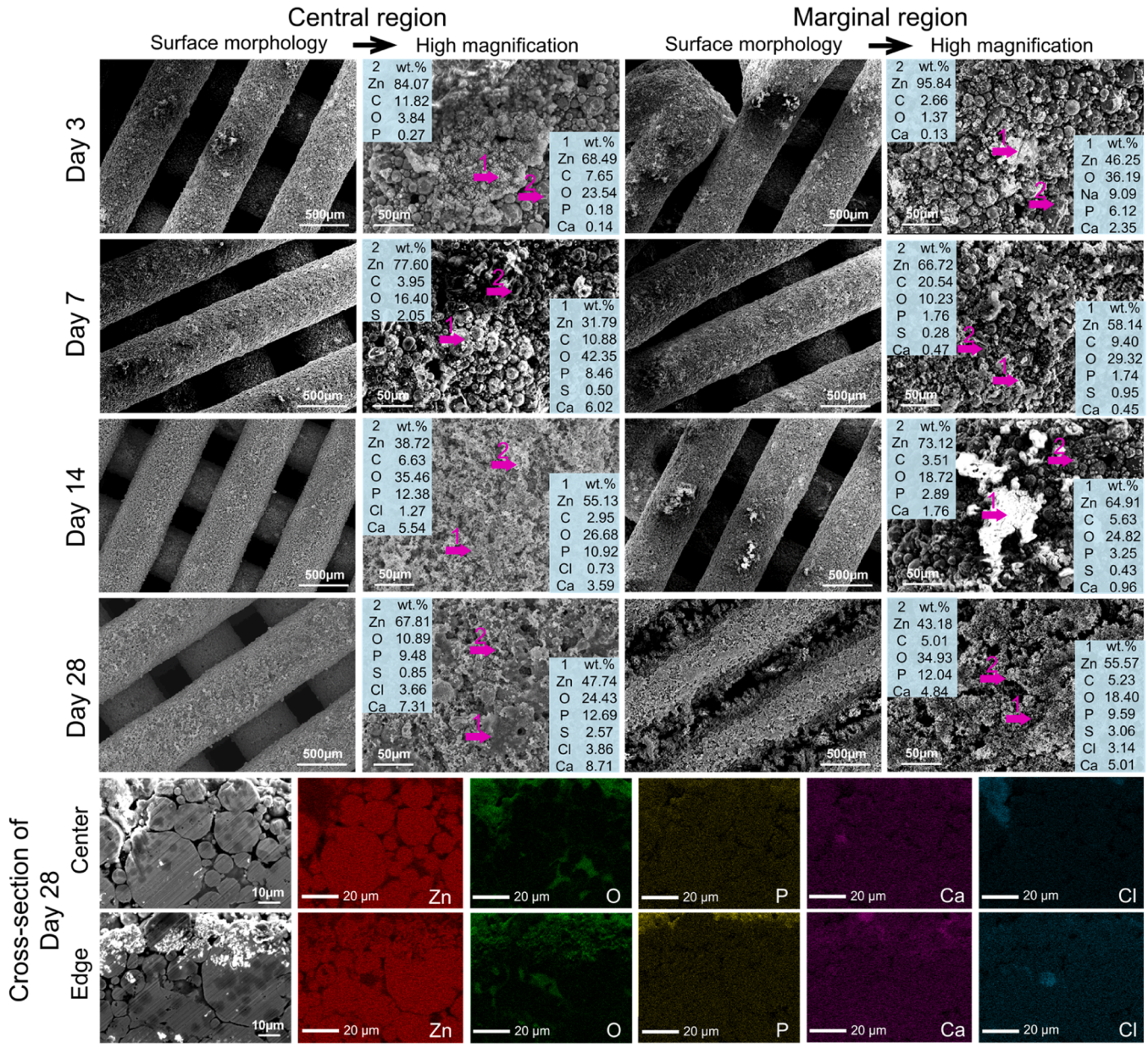

Fig. 9. SEM images and EDS analysis of the biodegradation products in the edge and central regions of the scaffold surfaces, as well as the cross-sections of the struts after *in vitro* immersion for different lengths of time.

respectively, which were close to the CR_W values obtained from the *in vitro* immersion tests. The Nyquist plot (Fig. 10b) showed that the diameter of the capacitance loop initially decreased, then began to increase steadily after 7 days, reaching its maximum on the 28th day. The fitted electrical equivalent circuit (EEC) data of the Zn scaffold samples (Fig. 10 b inset and Table 2) showed that both R_f and R_{ct} followed an overall trend of initially decreasing and then increasing as time lapsed, similar to the trend of the obtained R_p values (Fig. 10a).

3.5. Mechanical properties

The compression curves of the scaffolds sintered for 5 and 7 h exhibited similar trends: the specimens first underwent linear elastic deformation, followed by slight plastic deformation, then a plateau region, and finally fracture (Fig. 11a). In contrast, no clear plateau region was observed for the specimens after 3 h sintering. The specimens sintered for 5 and 7 h showed higher fracture strain values. The average yield strengths of the 3, 5, and 7 h-sintered specimens were 8.3 ± 0.7, 16.1 ± 1.3, and 9.2 ± 0.9 MPa, while the corresponding elastic moduli were 1.0 ± 0.1, 1.4 ± 0.1, and 0.7 ± 0.1 GPa, respectively (Fig. 11b). The specimens sintered at 5 h exhibited the maximum values of the mean yield strength and elastic modulus. Although the porosity of the Zn scaffold obtained in this study is relatively low (40 %), its mean yield strength is comparable to those of Zn scaffolds prepared by using other fabrication processes (Fig. 11c), indicating the need to strengthen the scaffolds in order to allow for higher porosity.

The average yield strength of the porous Zn specimens slightly decreased from 15.7 ± 0.8 MPa after 1 day of immersion to 14.5 ± 0.7

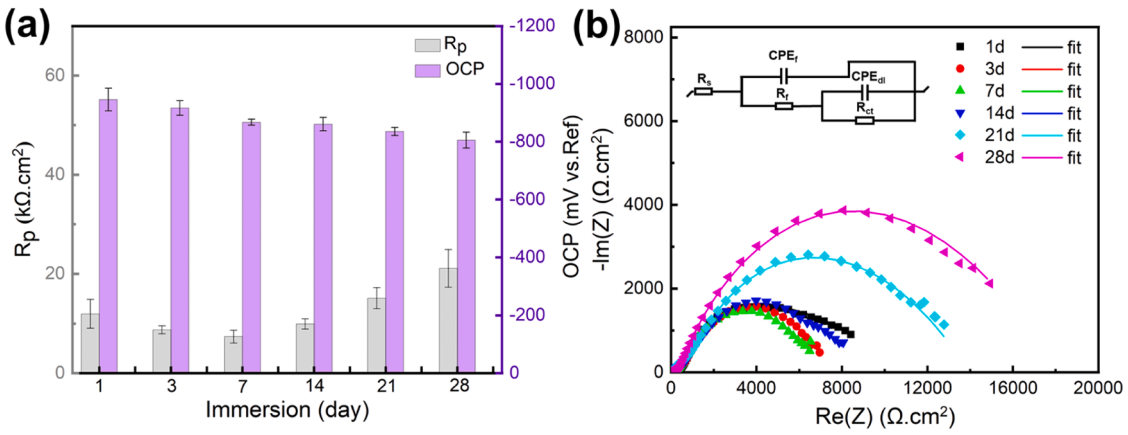

Fig. 10. Electrochemical characteristics of the porous Zn scaffolds at different time points: (a) OCP and R_p variations with time, (b) Nyquist plots with corresponding equivalent circuits.

Table 2
EIS fitting parameters of the Zn scaffolds after the tests at different time points.

Time d	R_s Ω•cm^2	CPE_f 10^{-6}• Ω^{-1}•cm^{-2}•s^{n1}	n_1	R_f kΩ•cm^2	CPE_{dl} 10^{-6}• Ω^{-1}•cm^{-2}•s^{n2}	n_2	R_{ct} kΩ•cm^2	$\chi 2 \times 10^{-3}$
1	32.0 ± 1.2	62.0 ± 0.3	0.27 ± 0.02	0.8 ± 0.2	12.4 ± 0.3	0.69 ± 0.05	10.5 ± 2.0	2.6 ± 0.3
3	50.1 ± 5.7	31.9 ± 0.2	0.38 ± 0.04	0.7 ± 0.1	31.6 ± 0.4	0.63 ± 0.01	6.8 ± 0.5	0.7 ± 0.1
7	21.8 ± 4.0	36.4 ± 0.4	0.34 ± 0.02	0.6 ± 0.2	31.4 ± 0.5	0.63 ± 0.02	6.5 ± 0.6	4.1 ± 0.2
14	23.2 ± 1.5	44.3 ± 0.7	0.36 ± 0.02	0.9 ± 0.2	11.3 ± 0.3	0.71 ± 0.08	7.8 ± 0.9	5.1 ± 0.4
21	23.3 ± 1.8	24.7 ± 0.4	0.41 ± 0.01	1.7 ± 0.4	5.7 ± 0.1	0.71 ± 0.06	12.0 ± 1.2	9.7 ± 0.4
28	33.4 ± 7.6	27.0 ± 0.6	0.36 ± 0.03	0.6 ± 0.3	33.4 ± 0.5	0.64 ± 0.02	17.8 ± 1.8	7.6 ± 0.1

Rs (solution resistance), CPE_f (surface film capacitance), R_f (surface film resistance), R_{ct} (charge transfer resistance) and CPE_{dl} (double layer capacitance)

MPa after 3 days of immersion (Fig. 11d). It declined sharply to 8.3 ± 0.4 MPa after 7 days of immersion. Finally, it decreased to 3.7 ± 0.3 MPa on the 28th day (Fig. 11e). Similarly, the elastic modulus slightly reduced from 1.4 ± 0.1 GPa after 1 day of immersion to 1.3 ± 0.1 GPa after 3 days of immersion. Then, the elastic modulus decreased approximately proportionally with time to 0.5 ± 0.1 GPa after 14 days

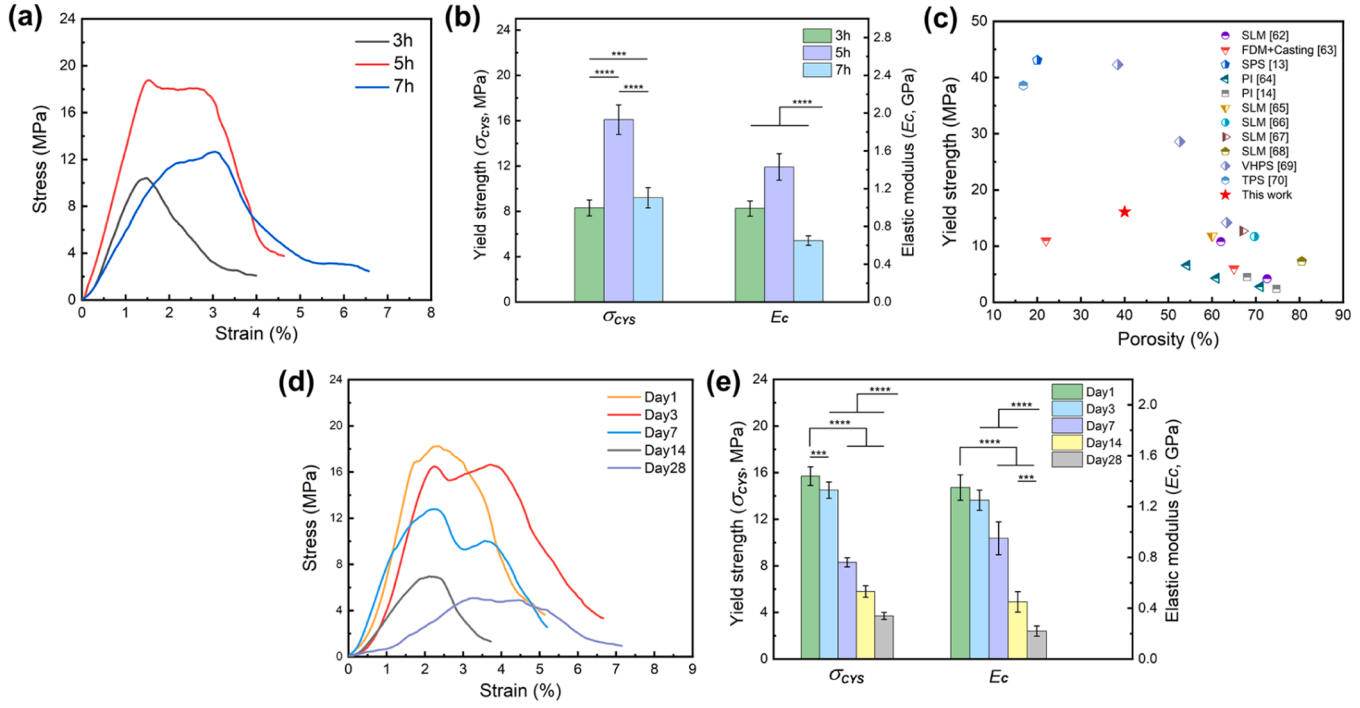

Fig. 11. (a) Compressive stress *versus* strain curves of the scaffolds after 3, 5, and 7 h sintering but prior to *in vitro* immersion, (b) histogram of the corresponding compressive yield strengths and elastic moduli, and (c) Ashby plot compiling porosity and yield strength values to compare the results of the present research with those of other porous Zn fabricated by using different fabricating processes (SLM-selective laser melting, FDM-fused deposition modeling, SPS-spark plasma sintering, PI-pressure infiltration, VHPS-vacuum heating-press sintering, TPS-thermal plasma spraying) [13,14,62–70]. Compressive mechanical properties of the Zn scaffolds after *in vitro* immersion: (d) stress-strain curves and (e) variations of yield strength and elastic modulus with immersion time.

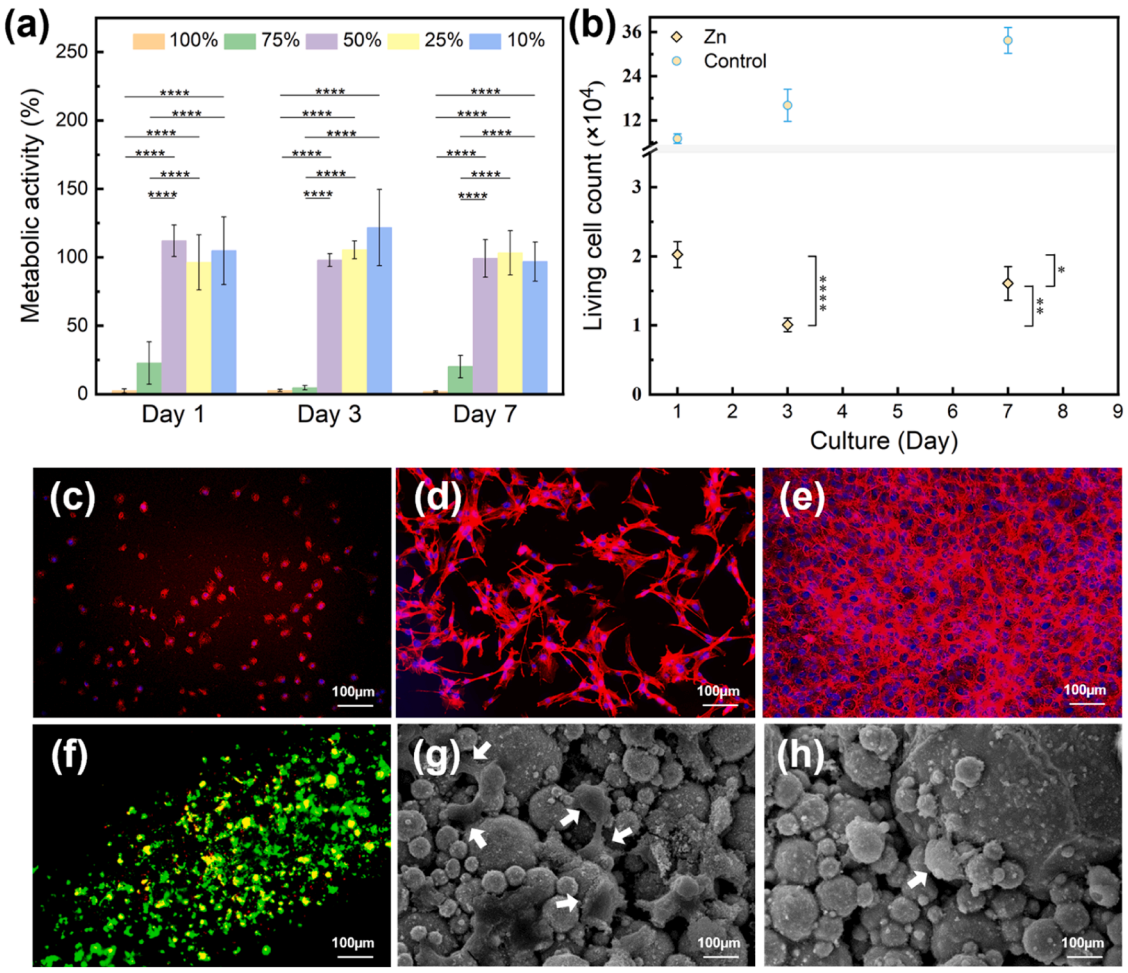

Fig. 12. *In vitro* biological evaluation of the Zn scaffolds: (a) metabolic activity of MC3T3-E1 preosteoblasts cultured in the different Zn extracts for 1, 3, and 7 days; (b) the numbers of live preosteoblasts after 1, 3, and 7 days of direct culture; (c-e) rhodamine phalloidin (red) and DAPI (blue) stained preosteoblasts after 7 days of indirect culture in (c) 100 %, (d) 75 %, (e) 50 % Zn extracts; (f) live/dead staining of preosteoblasts on the scaffolds after 3 days of culture; (g, h) SEM images of the cells on the scaffolds after 3 days of culture (cells are indicated by the white arrows).

of immersion. Finally, the elastic modulus reached 0.2 ± 0.1 GPa after 28 days of *in vitro* biodegradation.

3.6. *In vitro cytocompatibility*

Exposure to the 100 % Zn extract resulted in immediate cytotoxicity, with the metabolic activity reduced to just 2.4 ± 1.5 % after 24 h and almost no metabolically active cells remaining after 7 days of culture (Fig. 12a). When the Zn extract was diluted to 75 % of the original concentration, however, the metabolic activity was increased to 22.7 ± 15.5 % after 24 h of culture. After 72 h of culture, the metabolic activity of the MC3T3-E1 cells decreased to 4.7 ± 1.6 %, but by 7 days, the metabolic activity of the cells increased to 20.1 ± 8.2 %. When the Zn extract was further diluted to ≤ 50 %, the growth of preosteoblasts was only slightly inhibited, and the metabolic activity remained high (> 90 %) even after 7 days of culture. The morphology of MC3T3-E1 cells after 7 days of culture in different Zn extracts (Fig. 12c–e) supported the findings on the metabolic activity. The cells were relatively round and small in the 100 % extracts. By comparison, they showed a spread morphology in the 75 % extracts and in the 50 % extracts they were already confluent.

Direct seeding of preosteoblasts on the porous Zn scaffolds reduced the number of viable cells relative to the control samples (*i.e.*, 2.0 ± 0.2 (× 10^4) cells) after 24 h of culture (Fig. 12b). After 3 days of culture, the number of viable cells continued to decrease to 1.0 ± 0.1 (× 10^4) cells ($p < 0.0001$ *versus* 'Day 1'). However, on the 7th day of culture, the number of viable cells slightly increased to 1.6 ± 0.2 (× 10^4) ($p < 0.05$ *versus* 'Day 1' and $p < 0.01$ *versus* 'Day 3'). Live-dead staining results showed that after 3 days, the preosteoblasts were evenly distributed on the struts of the Zn scaffolds, with both live (green) and unhealthy/dead preosteoblasts (yellow or red) present (Fig. 12f). SEM imaging of the Zn scaffolds after 3 days of culture showed that some cells could spread and grow on the Zn particles and near the biodegradation products (Fig. 12g, h).

4. Discussion

4.1. *Sintering behavior and mechanism of the as-printed Zn scaffolds*

To elucidate the sintering mechanism of the Zn scaffolds fabricated *via* extrusion-based AM, it is essential to understand the actual sintering cycle experienced by the specimens, which deviates from the settings. Although the intended sintering temperature was set at 415 °C, just below the measured melting point of the Zn powder (418.4 °C), to maximize solid-phase diffusion and also maintain the structural integrity of the Zn scaffold throughout the sintering process, the actual sintering temperature of the samples fluctuated around 415 °C due to the unique heating pattern of the sintering furnace (Fig. 13a). In fact, the maximum sintering temperature (~ 421 °C) exceeded the melting point of Zn multiple times over a time span of nearly 60 min. As a result, the

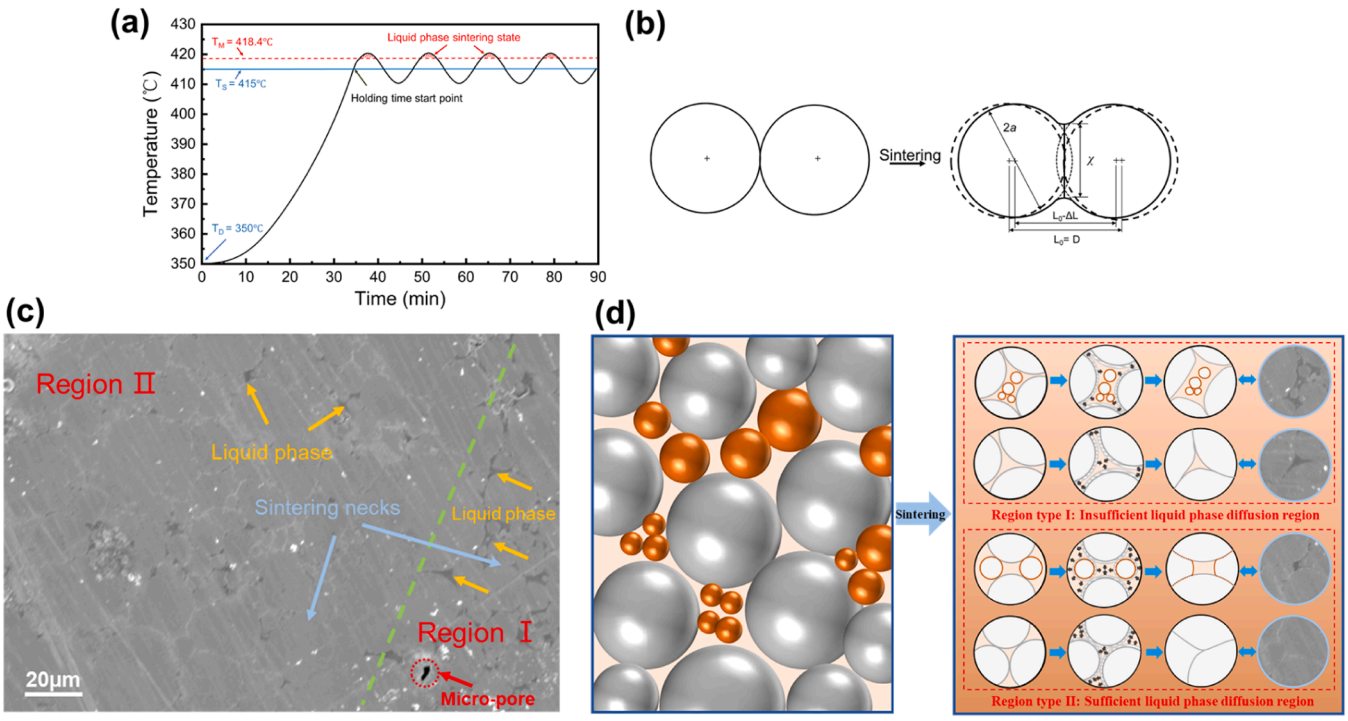

Fig. 13. Sintering behavior and mechanism analysis: (a) an illustration of the actual sintering temperature variation pattern, (b) two-particle sintering model for Zn powder, (c) the representative SEM image of the microstructure of the strut in the as-sintered Zn scaffolds, highlighting typical regions of insufficient and sufficient particle rearrangement and solution-reprecipitation, and (d) an illustration of the generation of insufficient and sufficient solution-reprecipitation, driven by the slight variations in local initial Zn powder packing density. In panel (c) and (d), the gray and orange colors are used solely to distinguish between larger and smaller Zn powder particles within a continuous size distribution, facilitating the visualization of their interaction and the resulting densification process during sintering.

unexpectedly high sintering temperature inevitably introduced liquid-phase sintering (indicated by the red dashed line in Fig. 13a), as evidenced by the severe collapse of the specimens sintered at 418 °C due to overheating (Section 3.2). The dramatic difference in sintering outcomes within a narrow temperature range is attributed to the hybrid solid-liquid phase sintering mechanism. The setpoint of 415 °C, coupled with inherent thermal fluctuations, ensures the generation of a critical volume of liquid phase necessary for effective particle rearrangement and bonding via solution-reprecipitation. Conversely, at 412 °C, the process remains dominated by solid-state diffusion, which provides insufficient bonding strength to prevent collapse of the porous structure. Therefore, it can be inferred that both solid-phase and liquid-phase sintering occurred when a sintering temperature of 415 °C was used to prepare the specimens.

The 'fusion quality' of the scaffolds, referring to the degree of densification within the individual struts, was critically examined. Although the relative density of the struts was not directly quantified, the SEM and micro-CT analyses (Figs. 4h, 6c) conclusively demonstrated a high level of strut consolidation with minimal internal porosity following the optimized sintering process. This enhanced densification, attributed to the hybrid solid-liquid phase sintering mechanism, confirmed that the struts themselves are sufficiently dense to provide mechanical integrity, fulfilling the primary objective of creating a robust porous scaffold. The microstructure of the sintered pure Zn scaffolds was further characterized, as shown in Fig. S3. The scaffolds exhibited a relatively uniform and equiaxed grain structure with an average grain size of approximately 4.5 μm (Fig. S3a and 3b). The present scaffolds showed no significant directional preference in grain morphology, which can be attributed to the isotropic nature of the sintering process. Furthermore, EDS elemental mapping confirmed the presence of residual binder, evidenced by a homogeneous distribution of C and O elements within the microstructure (Fig. S3c–f).

Bonding between contacting Zn particles at sintering necks is a prominent aspect of solid-phase sintering. The bonds reduce the surface energy by removing the free surface, with the secondary elimination of grain boundary area *via* grain growth [71,72]. Grain boundary (GB) diffusion and surface diffusion are two primary mechanisms driving mass transport when forming growth necks [73]. The two-particle sintering model [74] (Fig. 13b) predicts the evolution of sintering neck growth between two Zn particles. Both particles are assumed to be slightly attached in the necking area at the beginning of sintering. Thus, the growth rate of the sintering neck driven by GB diffusion is given as [73]:

$$\frac{x}{a} = \left(\frac{96 D_{gb}\gamma\Omega\delta_{gb}}{kTa^4}\right)^{1/6} t^{1/6} \tag{7}$$

The growth rate of the sintering neck driven by surface diffusion can be expressed as:

$$\frac{x}{a} = \left(\frac{56 D_s\gamma\Omega\delta_s}{kTa^4}\right)^{1/7} t^{1/7} \tag{8}$$

where x is the length of the sintering neck, a is the particle radius, D_{gb} and D_s are the diffusion coefficients for GB and surface diffusion, k is the Boltzmann constant, γ is the surface energy, Ω is the volume of the diffusing vacancy, $\delta_{gb,}$ and δ_s are the thicknesses for GB and surface diffusion, T is the sintering temperature, and t is the sintering time. A longer sintering time allows for more diffusion to occur, thereby strengthening the interfacial bonding between Zn particles through the growth of solid-phase sintering necks. At the same time, elevated temperatures above the melting point are unfavorable for the stability of these sintering necks.

The liquid phase must have repeatedly appeared throughout the sintering cycle (above 418.4 °C) (Fig. 13c), resulting in accelerated densification with only a few micro-voids retained. This is attributed to the capillary forces [75] from the wetting liquid that act on the solid Zn particles to minimize interfacial areas, reducing porosity through

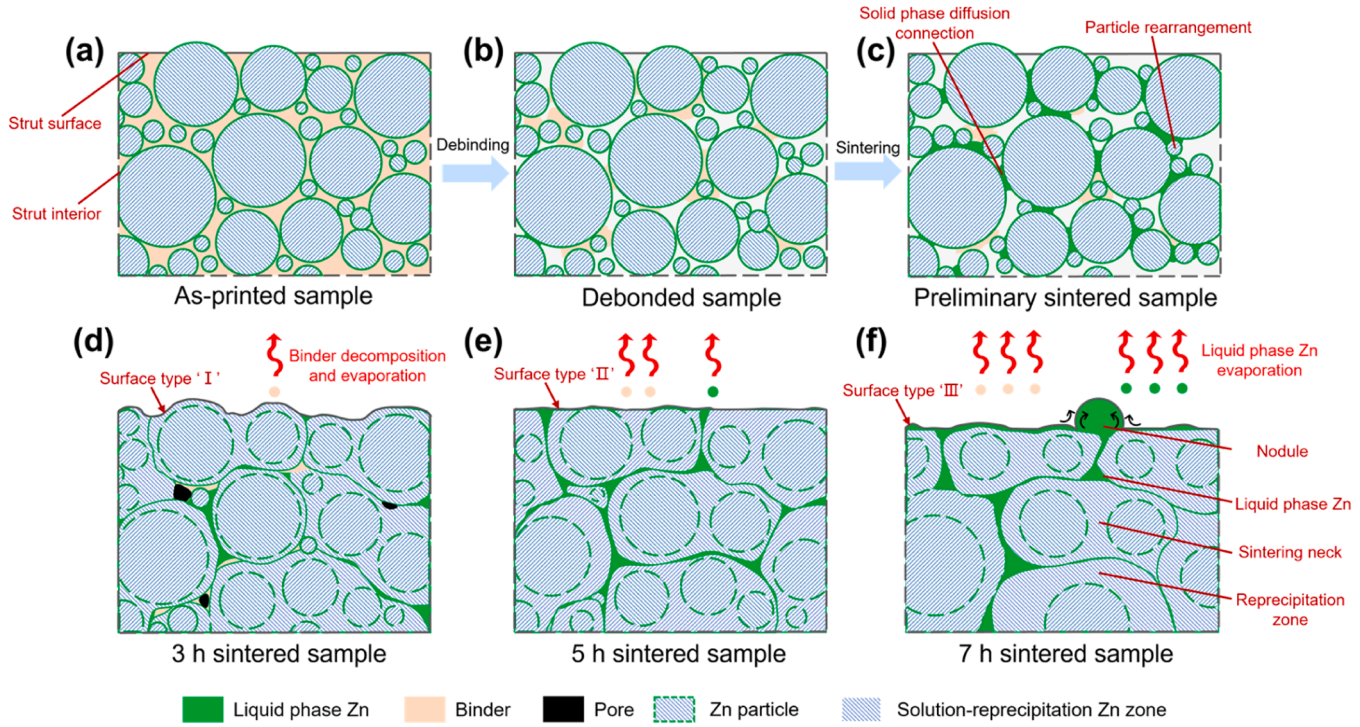

Fig. 14. Illustration of the sintering mechanisms of the Zn scaffolds fabricated by extrusion-based AM.

particle rearrangement (*i.e.*, the first stage in liquid-phase sintering) [76]. In addition, an elevated diffusion rate in the liquid state enables faster bonding and densification compared to the equivalent solid-phase sintering process. In the as-sintered samples, two distinct regions (labeled as 'Region I' and 'Region II) were observed, showing non-uniformity in the volume of the liquid Zn phase between solid Zn particles, resulting from a non-uniform distribution of smaller particles and also from non-uniform solution-reprecipitation [77] (*i.e.*, the second stage during liquid-phase sintering), and exhibiting varied densification effects affected by local Zn particle packing density [78]. A powder with a broad particle size distribution is expected to have a high packing density [79,80], but packing may not be uniform everywhere. Any inhomogeneous initial packing of powder particles can strongly influence densification kinetics, including densification during the solution-reprecipitation stage [81], with more homogeneously packed powder particles densifying faster. The D10 value of the Zn powder used in this study is only 8.8 μm, resulting in a strong filling effect to enhance packing density. Fig. 13d illustrates the possible densification process driven by insufficient and sufficient particle rearrangement and solution-precipitation caused by different local Zn particle packing densities. In addition, the total sintering time significantly influences the extent of liquid sintering, as a longer sintering time allows for more diffusion and densification, resulting in a larger volume of liquid Zn [82]. The differences in the volume of the liquid Zn phase between solid Zn particles as a function of sintering time, varying from 3 to 7 h, can be observed in Fig. 4g–i. Fig. S4 further presents the calculated area fractions of the liquid Zn phase in the selected area within the polished struts sintered for 3, 5, and 7 h, which were 1.8, 3.0, and 6.8 %, respectively. Increasing the sintering time, resulting in a larger liquid phase fraction, effectively reduced the number and size of pores (Fig. 6) and improved the sintering quality of the strut surface as more liquid Zn filled the interconnected microporous network [45]. However, the formation of nodules and severe Zn evaporation (Fig. 4i) due to the excessive generation of liquid Zn, as well as the resultant decrease in the compression strength of the specimens sintered for 7 h (Fig. 11a), means the moderate sintering time (5 h in the present research) can lead to a better balance in sintering defects, surface quality, and mechanical properties. Based on the above discussion, Fig. 14 illustrates the mechanisms of sintering that involve both the solid and liquid states, in relation to varying sintering times.

4.2. *In vitro* biodegradation behavior and mechanism

The static *in vitro* corrosion rates (CR_W) of the Zn scaffolds (0.06 ± 0.01 mm/y at day 1 and 0.03 ± 0.01 mm/y at day 28) (Fig. 7g) are comparable to those of cast bulk zinc (*i.e.*, 0.008 - 0.03 mm/y) [61,83,84] and hot-extruded bulk Zn (*i.e.*, 0.012 - 0.104 mm/y) [85–90], but much lower than those of porous Zn (*i.e.*, 0.125 - 4.24 mm/y) [13,62,63] with porosity varying in the range of 11.3 % – 65 %. The low static *in vitro* corrosion rates of the Zn scaffolds are expected to leave room for the integration of alloying elements or bioactive agents into the Zn matrix for enhanced mechanical properties and/or biocompatibility because alloying or compositing tends to accelerate biocorrosion. In addition to the influence of SBF solution type and the variations in microstructural features (*e.g.*, grain size [59] and texture [91]) induced during material processing on the *in vitro* degradation rate, the two primary factors influencing the *in vitro* degradation rate are the overall porosity of the scaffold and the microscale porosity within the scaffold struts. With the optimized process parameters used in sintering when a small fraction of the liquid phase existed, only a minimum number of internal pores remained in the struts of the scaffolds after 5 h of sintering (Figs. 4h and 6c). This is a major improvement from the extensive microporous networks observed in the extrusion-based AM pure iron [45] and pure magnesium [40], and could significantly improve the mechanical properties of Zn-based biomaterials, which is welcome given that the mechanical properties of the base metal are significantly lower than those of Fe and Mg. Moreover, when the well-consolidated struts in the AM Zn scaffolds were in contact with the r-SBF, a robust, dense surface layer could form, which acts as an effective physical barrier to further corrosion, thereby reducing the invasion of the r-SBF and minimizing the potential for creating sites favorable for autocatalytic corrosion, typically crevice corrosion [92], caused by randomly interconnected micropores where the r-SBF could be entrapped. The lower macroporosity of the scaffolds sintered for 5 h (40 %) and extremely low

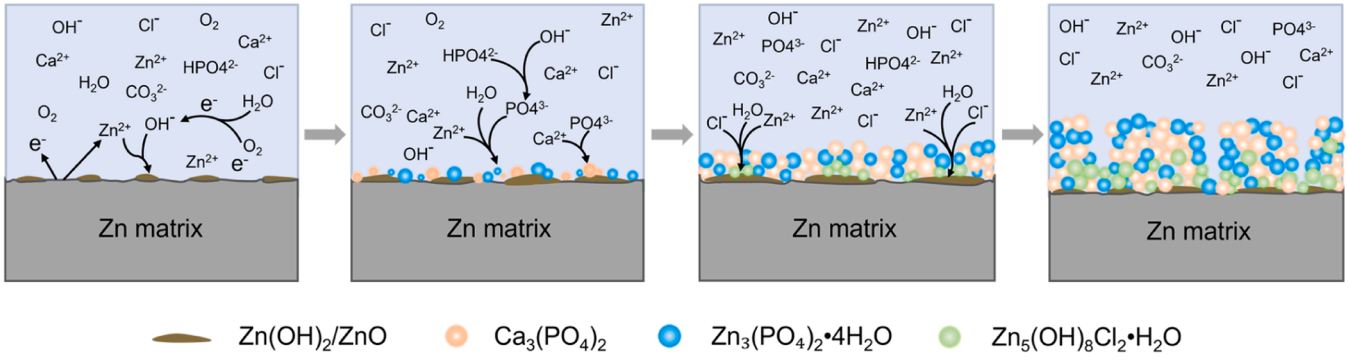

Fig. 15. An illustration of the *in vitro* corrosion biodegradation mechanism of the Zn scaffolds fabricated by extrusion-based AM. To simplify the illustration, the porous Zn strut is considered the dense and smooth Zn matrix.

microporosity in the struts could explain their relatively low *in vitro* biodegradation rate.

From the electrochemical perspective, the continuous decrease of OCP with time (Fig. 10a) indicates that the material was continuously oxidized in the r-SBF solution, and the surface of the porous Zn must have been gradually covered by the biodegradation products, resulting in progressive decreases in electrode potential [93]. The total resistance value R_t (defined by $R_t = R_f + R_{ct}$) can be used to evaluate the corrosion resistance of the Zn specimens [94], and the trend of R_t is consistent with that of R_p. The initial high R_f and R_{ct} values (at day 1) are attributed to the rapid formation of an initial, protective biodegradation product layer (*e.g.*, ZnO and Zn(OH)₂) on the scaffold surface during the 1-hour OCP stabilization period in r-SBF. This newly formed layer, acted as the primary barrier impeding direct contact between the electrolyte and the Zn matrix, thus hindering charge transfer [95]. As corrosion progresses (between days 3 and 7), this oxide film breaks down due to the continuous attack of aggressive ions, such as Cl^-, exposing the fresh Zn matrix. At the same time, the newly formed corrosion layer, containing, *e.g.*, ZnO and $Zn(OH)_2$, is not dense yet and allows easy electrolyte penetration, which reduces R_t by enhancing the exchange of ions between the electrolyte and biodegradation products. With further corrosion (between days 7 and 28), the corrosion layer thickens and densifies and displays even passivation behavior (evidenced by the current plateaus in anodic polarization, Fig. S2) [96], which restricts electrolyte penetration and limits active corrosion sites [97], causing R_t to rise.

The mechanisms of the biodegradation of the Zn scaffold in the r-SBF, disregarding the initial presence of an oxide film, can be described as follows. During the initial stage, when the Zn scaffold meets the water and dissolved oxygen in the r-SBF, the Zn corrodes through the reactions:

Anodic reaction: $Zn \rightarrow Zn^{2+} + 2e^-$

Cathodic reaction: $O_2 + H_2O + 4e^- \rightarrow 4OH^-$

$2H_2O + 2e^- \rightarrow 2OH^- + H_2$

As OH^- is generated and accumulated in the solution and Zn^{2+} is continuously released, the biodegradation products $Zn(OH)_2$ and ZnO are first formed:

$Zn^{2+} + 2OH^- \rightarrow Zn(OH)_2$

$Zn^{2+} + 2OH^- \rightarrow ZnO + 2H_2O$

The weak alkaline environment (pH 7.8 ± 0.1 at day 7, Fig. 7e) in the initial stage of Zn scaffold degradation is conducive to the generation of PO_4^{3-} in the solution. At the same time, due to the high Ca^{2+} level (73.3 ± 1.1 mg/L) in the r-SBF solution at the beginning, $Ca_3(PO_4)_2$ nucleate and generate:

$HPO_4^{2-} + OH^- \rightarrow PO_4^{3-} + H_2O$

$Ca^{2+} + PO_4^{3-} \rightarrow Ca_3(PO_4)_2$

With the increase in immersion time, the alkalinity of the solution intensifies, and Zn^{2+} is continuously released, $Zn_3(PO_4)_2 \bullet 4H_2O$ begins to precipitate:

$3Zn^{2+} + 2PO_4^{3-} + 4H_2O \rightarrow Zn_3(PO_4)_2 \cdot 4H_2O$

The infrared absorption peaks of PO_4^{3-} (Fig. 8a) and the P2p peaks at 133 and 134 eV (Fig. 8e and f) appeared on the 14th and 28th days, confirming the occurrence of these reactions. Additionally, the presence of Cl^- in the r-SBF induces a reaction with the biodegradation product Zn $(OH)_2$ to form chloride salts:

$4ZnO + 4H_2O + Zn^{2+} + 2Cl^- \rightarrow 4Zn(OH)_2 \cdot ZnCl_2$

Based on the reactions above, Fig. 15 depicts the possible corrosion mechanism of the Zn scaffolds in the r-SBF.

4.3. *Bone-mimicking mechanical properties*

Over the 28-day *in vitro* biodegradation period, the mechanical properties of the Zn scaffolds remained within the range of those of the trabecular bone (*i.e.*, yield strength = 0.2–80 MPa; elastic modulus = 0.5–20 GPa) [98]. These values indicate the need to enhance the mechanical properties so that the scaffolds can withstand cyclic loading in a corrosive environment, as expected *in vivo*, and even substitute load-bearing bones. It is, however, important to realize that the mechanical properties of porous scaffolds increase 2–7 times as a result of bone regeneration into the pores of the microarchitected biomaterial [99]. There may, therefore, not be a need for very high level of mechanical properties for all applications.

The stress-strain curves showed that the Zn scaffolds after immersion (Fig. 11d) did not exhibit the typical mechanical properties of a ductile material but instead displayed rapid mechanical collapse after reaching the peak stress, similar to the compression characteristics of many other Zn and Zn alloy scaffolds [22,100–102]. This brittleness likely arises from incomplete fusion of Zn particles, hindering load transfer and causing stress concentrations at bonding interfaces. This requires redesigning the scaffold architecture to eliminate stress concentration sites and, consequently, enhance its load-carrying capability. It should be noted that the compressive properties reported herein were evaluated along the build direction (Z-axis), which represents the most critical loading scenario; however, the potential anisotropy arising from the layer-by-layer fabrication process warrants further investigation.

As the immersion time increased, the yield strength and elastic modulus of the porous Zn scaffolds continued to decrease. This behavior differs from the paradigms of mechanical property changes over time, reported in the literature regarding the *in vitro* biodegradation of the porous Mg-Zn alloy [39], pure Fe [45], and LPBF porous Zn [64], which

typically exhibit a temporary increase in mechanical strength during initial immersion. The formation of biodegradation products causes load sharing between the scaffold and the biodegradation products, thereby increasing mechanical strength. Conversely, the dissolution of the scaffold leads to a decrease in mechanical strength. In our study, the biodegradation products generated in a smaller volume during Zn degradation had a limited strengthening effect, resulting in a consistent decline in yield strength. In other words, this disrupted the typical compensatory mechanism, resulting in steep declines in yield strength and elastic modulus on days 7 and 14. However, the continued accumulation of the biodegradation products, indeed, helped sustain the compressive load by day 28, as reflected by the compressive fracture strain of the scaffold after *in vitro* immersion for 28 days (~3.3 %), which was higher than the fracture strains at the previous time points (~2 %). This was because the formation of the biodegradation products filled the micropores inside the struts and covered the struts, decreasing the porosity of the entire scaffold and enabling it to withstand the loads, thereby delaying mechanical collapse. In addition, the observed sharp decline in compressive strength after immersion, despite the low overall mass loss, can be attributed to localized corrosion at critical load-bearing points, particularly the sintering necks between particles. The failure of these strategically located connections triggers cascading structural collapse, explaining the disproportionate loss of mechanical integrity relative to the minimal bulk material dissolution (Day 28).

4.4. Cytocompatibility of the Zn scaffolds

Firstly, we performed indirect cytotoxicity tests according to the ISO 10993–5 standard [103]. Therefore, a range of extract dilutions were used to study the sensitivity of the cells to the extracts [30,104–106]. The 100 % Zn extracts exhibited severe toxicity (level 4), resulting in almost no metabolically active cells, whereas the 75 % Zn extracts showed moderate toxicity (level 3) and the ≤ 50 % Zn extracts showed only slight toxicity (level 1) or no toxicity (level 0). Yamamoto et al. [107] reported that the IC50 of Zn^{2+} (*i.e.*, the half-maximal inhibitory concentration) for MC3T3-E1 cells was 90 μM. In our study, the Zn^{2+} concentration in the undiluted extract (100 %) was measured to be 118.5 μM, exceeding the cell tolerance limit and causing cytotoxicity. The 50 % extract (with a Zn^{2+} concentration of 59.3 μM) and the more diluted ones posed no significant cytotoxic effects to MC3T3-E1 cells, as evidenced by their increased metabolic activity and ability to proliferate in the first week of culture. Zn ions are known for positively affecting osteoblast proliferation at a low concentration (*i.e.*, 50 μM) [108]. The favorable cytocompatibility observed in this study, evidenced by the high metabolic activity (>90 %) in the extracts diluted to ≤50 % and successful cell adhesion and spreading in direct culture, also indicates that the trace carbonaceous residues present after sintering did not elicit significant cytotoxic effects under the testing conditions. This is supported by the fact that the source polymer, PVP, is widely acknowledged for its biocompatibility and low cytotoxicity [109,110]. To minimize any potential influence from the organic residues in future work, strategies such as employing another binder system with a cleaner burnout profile or optimizing the thermal debinding cycle could be implemented.

The direct cultures revealed that the porous Zn scaffolds were slightly cytotoxic, indicating that modification of the scaffold's composition is necessary to enhance its cytocompatibility. The main reasons for reduced cell viability and adhesion include the excessive release of Zn^{2+} ions, increased local pH, changes in surface morphology and chemistry, and detaching of the corrosion layer [111]. It is essential to note that the static *in vitro* environment used in the present study cannot replicate the dynamic *in vivo* environment. In the static environment, cells are exposed to elevated concentrations of Zn^{2+} released from the surface of the Zn scaffolds. Nevertheless, MC3T3-E1 cells could still be observed after 3 days of direct culture, showing a spread morphology especially between the biodegradation products and fused Zn particles, indicating their adaptation potential to the degrading surface.

5. Conclusions

In this study, biodegradable Zn scaffolds were successfully fabricated for the first time using extrusion-based AM after the ink formulation, printing, and sintering processes were optimized. The resulting Zn scaffolds were thoroughly evaluated for their potential application as biodegradable bone substitutes. These results establish extrusion-based AM as a viable route for fabricating Zn scaffolds with tailored porosity, biodegradation, bone-like properties, and controlled cytotoxicity, advancing the foundational development of Zn-based biodegradable implants and paving the way for future *in vivo* evaluation. Room for improvement in mechanical properties and cytocompatibility is also identified.

1. An ink composition with 53 vol. % Zn powder loading, a sintering temperature of 415 °C, and a sintering time of 5 h were found to lead to optimum Zn porous scaffolds, achieving a yield strength of 16.1 ± 1.3 MPa and an elastic modulus of 1.4 ± 0.1 GPa, being comparable to the mechanical properties of the cancellous bone.
2. The co-occurrence of solid-state and liquid-phase sintering resulted in the densification of the struts with minimum pore defects, Zn evaporation, and enhanced strut fidelity.
3. The *in vitro* biodegradation rate of the Zn scaffolds increased and then decreased over the 28-day immersion period, influenced by the formation of a dense biodegradation product layer consisting of ZnO, $Ca_3(PO_4)_2$, $Zn_3(PO_4)_2{\bullet}4H_2O$, and $Zn_5(OH)_8Cl_2{\bullet}H_2O$. An *in vitro* biodegradation rate of 0.03 ± 0.01 mm/y at day 28 was measured for the Zn scaffolds.
4. The biodegradable Zn scaffolds exhibited good cytocompatibility for MC3T3-E1 cells when the Zn concentration in the extracts was below 59.3 μM, although slight cytotoxicity was observed in the direct cultures. The MC3T3-E1 cells could attach and spread between the Zn particles and biodegradation products.

CRediT authorship contribution statement

Keyu Chen: Writing – original draft, Methodology, Investigation, Formal analysis, Data curation, Conceptualization. **Jiahui Dong:** Investigation, Formal analysis. **Niko Eka Putra:** Investigation, Formal analysis. **Jinlai Li:** Methodology, Investigation, Formal analysis, Conceptualization. **Maria Klimopoulou:** Methodology, Formal analysis. **Marius A. Leeflang:** Methodology, Investigation. **Lidy Elena Fratila-Apachitei:** Writing – review & editing, Investigation, Conceptualization. **Jie Zhou:** Writing – review & editing, Validation, Supervision, Conceptualization. **Amir A. Zadpoor:** Writing – review & editing, Validation, Supervision, Conceptualization.

Declaration of competing interest

The authors declare that they have no known competing financial interests or personal relationships that could have appeared to influence the work reported in this paper.

Acknowledgments

K.C. thanks the China Scholarship Council (CSC) for financial support. Mr. Ruud Hendrikx, from the Department of Materials Science and Engineering, Delft University of Technology, is acknowledged for the XRD analysis. Mr. Michel van den Brink, from the Department of Process and Energy, Delft University of Technology, is acknowledged for the ICP-OES analysis. The authors thank Mr. Bart Boshuizen from the Department of Chemical Engineering, Delft University of Technology, for his assistance with the XPS measurements. The assistance of Mrs. Agnieszka Kooijman at the Department of Materials Science and

Engineering, Delft University of Technology, in the electrochemical tests is also greatly appreciated.

Supplementary materials

Supplementary material associated with this article can be found, in the online version, at doi:10.1016/j.actbio.2026.01.039.

References

[1] W. Wang, K.W.K. Yeung, Bone grafts and biomaterials substitutes for bone defect repair: a review, Bioact. Mater. 2 (2017) 224–247, https://doi.org/10.1016/j.bioactmat.2017.05.007.

[2] K. Chen, J. Dong, N.E. Putra, L.E. Fratila-Apachitei, J. Zhou, A.A. Zadpoor, Additively manufactured function-tailored bone implants made of graphene-containing biodegradable metal matrix composites, Prog. Mater. Sci. 155 (2026) 101517, https://doi.org/10.1016/j.pmatsci.2025.101517.

[3] A.J.T. Teo, A. Mishra, I. Park, Y.J. Kim, W.T. Park, Y.J. Yoon, Polymeric biomaterials for medical implants and devices, ACS Biomater. Sci. Eng. 2 (2016) 454–472, https://doi.org/10.1021/acsbiomaterials.5b00429.

[4] J. Chlopek, P. Rosol, A. Morawska-Chochol, Durability of polymer-ceramics composite implants determined in creep tests, Compos. Sci. Technol. 66 (2006) 1615–1622, https://doi.org/10.1016/j.compscitech.2005.11.016.

[5] S.M. Ahmadi, R. Hedayati, Y. Li, K. Lietaert, N. Tümer, A. Fatemi, C.D. Rans, B. Pouran, H. Weinans, A.A. Zadpoor, Fatigue performance of additively manufactured meta-biomaterials: the effects of topology and material type, Acta Biomater. 65 (2018) 292–304, https://doi.org/10.1016/j.actbio.2017.11.014.

[6] R. Wauthle, J. van der Stok, S. Amin Yavari, J. Van Humbeeck, J.P. Kruth, A. A. Zadpoor, H. Weinans, M. Mulier, J. Schrooten, Additively manufactured porous tantalum implants, Acta Biomater. 14 (2015) 217–225, https://doi.org/10.1016/j.actbio.2014.12.003.

[7] J. Chen, J. Chen, H. Wang, L. He, B. Huang, S. Dadbakhsh, P. Bartolo, Fabrication and development of mechanical metamaterials via additive manufacturing for biomedical applications: a review, Int. J. Extrem. Manuf. 7 (2024) 012001, https://doi.org/10.1088/2631-7990/ad88e3.

[8] C. Li, C. Guo, V. Fitzpatrick, A. Ibrahim, M.J. Zwierstra, P. Hanna, A. Lechtig, A. Nazarian, S.J. Lin, D.L. Kaplan, Design of biodegradable, implantable devices towards clinical translation, Nat. Rev. Mater. 5 (2020) 61–81, https://doi.org/10.1038/s41578-019-0150-z.

[9] P. Li, J. Dai, Y. Li, D. Alexander, J. Čapek, J. Geis-Gerstorfer, G. Wan, J. Han, Z. Yu, A. Li, Zinc based biodegradable metals for bone repair and regeneration: bioactivity and molecular mechanisms, Mater. Today Bio 25 (2024) 100932, https://doi.org/10.1016/j.mtbio.2023.100932.

[10] X. Wen, J. Wang, X. Pei, X. Zhang, Zinc-based biomaterials for bone repair and regeneration: mechanism and applications, J. Mater. Chem. B 11 (2023) 11405–11425, https://doi.org/10.1039/D3TB01874A.

[11] L. Zhu, D. Luo, Y. Liu, Effect of the nano/microscale structure of biomaterial scaffolds on bone regeneration, Int. J. Oral Sci. 12 (2020) 1–15, https://doi.org/10.1038/s41368-020-0073-y.

[12] S.A.M. Tofail, E.P. Koumoulos, A. Bandyopadhyay, S. Bose, L. O'Donoghue, C. Charitidis, Additive manufacturing: scientific and technological challenges, market uptake and opportunities, Mater. Today 21 (2018) 22–37, https://doi.org/10.1016/j.mattod.2017.07.001.

[13] J. Čapek, E. Jablonská, J. Lipov, T.F. Kubatík, D. Vojtěch, Preparation and characterization of porous zinc prepared by spark plasma sintering as a material for biodegradable scaffolds, Mater. Chem. Phys. 203 (2018) 249–258, https://doi.org/10.1016/j.matchemphys.2017.10.008.

[14] Y. Hou, G. Jia, R. Yue, C. Chen, J. Pei, H. Zhang, H. Huang, M. Xiong, G. Yuan, Synthesis of biodegradable Zn-based scaffolds using NaCl templates: relationship between porosity, compressive properties and degradation behavior, Mater. Charact. 137 (2018) 162–169, https://doi.org/10.1016/j.matchar.2018.01.033.

[15] F. Meng, Y. Du, Research progress on laser powder bed fusion additive manufacturing of zinc alloys, Materials 17 (2024) 4309, https://doi.org/10.3390/ma17174309.

[16] C.N. Kelly, T. Wang, J. Crowley, D. Wills, M.H. Pelletier, E.R. Westrick, S. B. Adams, K. Gall, W.R. Walsh, High-strength, porous additively manufactured implants with optimized mechanical osseointegration, Biomaterials 279 (2021) 121206, https://doi.org/10.1016/j.biomaterials.2021.121206.

[17] D. Gu, X. Shi, R. Poprawe, D.L. Bourell, R. Setchi, J. Zhu, Material-structure-performance integrated laser-metal additive manufacturing, Science 372 (2021), https://doi.org/10.1126/science.abg1487 eabg1487.

[18] D. Zhao, H. Liang, C. Han, J. Li, J. Liu, K. Zhou, C. Yang, Q. Wei, 3D printing of a titanium-tantalum Gyroid scaffold with superb elastic admissible strain, bioactivity and *in-situ* bone regeneration capability, Addit. Manuf. 47 (2021) 102223, https://doi.org/10.1016/j.addma.2021.102223.

[19] K. Lietaert, A.A. Zadpoor, M. Sonnaert, J. Schrooten, L. Weber, A. Mortensen, J. Vleugels, Mechanical properties and cytocompatibility of dense and porous Zn produced by laser powder bed fusion for biodegradable implant applications, Acta Biomater. 110 (2020) 289–302, https://doi.org/10.1016/j.actbio.2020.04.006.

[20] F. Guaglione, L. Caprio, B. Previtali, A.G. Demir, Single point exposure LPBF for the production of biodegradable Zn-alloy lattice structures, Addit. Manuf. 48 (2021) 102426, https://doi.org/10.1016/j.addma.2021.102426.

[21] S. Li, H. Yang, X. Qu, Y. Qin, A. Liu, G. Bao, H. Huang, C. Sun, J. Dai, J. Tan, J. Shi, Y. Guan, W. Pan, X. Gu, B. Jia, P. Wen, X. Wang, Y. Zheng, Multiscale architecture design of 3D printed biodegradable Zn-based porous scaffolds for immunomodulatory osteogenesis, Nat. Commun. 15 (2024) 3131, https://doi.org/10.1038/s41467-024-47189-5.

[22] D. Zhao, K. Yu, T. Sun, X. Jing, Y. Wan, K. Chen, H. Gao, Y. Wang, L. Chen, X. Guo, Q. Wei, Material–structure–function integrated additive manufacturing of degradable metallic bone implants for load-bearing applications, Adv. Funct. Mater. 33 (2023) 2213128, https://doi.org/10.1002/adfm.202213128.

[23] P. Wen, L. Jauer, M. Voshage, Y. Chen, R. Poprawe, J.H. Schleifenbaum, Densification behavior of pure Zn metal parts produced by selective laser melting for manufacturing biodegradable implants, J. Mater. Process. Technol. 258 (2018) 128–137, https://doi.org/10.1016/j.jmatprotec.2018.03.007.

[24] M. Montani, A.G. Demir, E. Mostaed, M. Vedani, B. Previtali, Processability of pure Zn and pure Fe by SLM for biodegradable metallic implant manufacturing, Rapid Prototyp. J. 23 (2017) 514–523, https://doi.org/10.1108/RPJ-08-2015-0100.

[25] A.G. Demir, L. Monguzzi, B. Previtali, Selective laser melting of pure Zn with high density for biodegradable implant manufacturing, Addit. Manuf. 15 (2017) 20–28, https://doi.org/10.1016/j.addma.2017.03.004.

[26] Z.Z. Shi, X.X. Gao, H.J. Zhang, X.F. Liu, H.Y. Li, C. Zhou, Y.X. Yin, L.N. Wang, Design biodegradable Zn alloys: second phases and their significant influences on alloy properties, Bioact. Mater. 5 (2020) 210–218, https://doi.org/10.1016/j.bioactmat.2020.02.010.

[27] K. Chen, X. Gu, Y. Zheng, Feasibility, challenges and future prospects of biodegradable zinc alloys as orthopedic internal fixation implants, Smart Mater. Manuf. 2 (2024) 100042, https://doi.org/10.1016/j.smmf.2023.100042.

[28] A. Liu, Y. Qin, J. Dai, F. Song, Y. Tian, Y. Zheng, P. Wen, Fabrication and performance of Zinc-based biodegradable metals: from conventional processes to laser powder bed fusion, Bioact. Mater. 41 (2024) 312–335, https://doi.org/10.1016/j.bioactmat.2024.07.022.

[29] X. Jin, D. Xie, Z. Zhang, A. Liu, M. Wang, J. Dai, X. Wang, H. Deng, Y. Liang, Y. Zhao, P. Wen, Y. Li, *In vitro* and *in vivo* studies on biodegradable Zn porous scaffolds with a drug-loaded coating for the treatment of infected bone defect, Mater. Today Bio 24 (2024) 100885, https://doi.org/10.1016/j.mtbio.2023.100885.

[30] D. Xia, Y. Qin, H. Guo, P. Wen, H. Lin, M. Voshage, J.H. Schleifenbaum, Y. Cheng, Y. Zheng, Additively manufactured pure zinc porous scaffolds for critical-sized bone defects of rabbit femur, Bioact. Mater. 19 (2023) 12–23, https://doi.org/10.1016/j.bioactmat.2022.03.010.

[31] H. Yang, B. Jia, Z. Zhang, X. Qu, G. Li, W. Lin, D. Zhu, K. Dai, Y. Zheng, Alloying design of biodegradable zinc as promising bone implants for load-bearing applications, Nat. Commun. 11 (2020) 401, https://doi.org/10.1038/s41467-019-14153-7.

[32] H. Kabir, K. Munir, C. Wen, Y. Li, Recent research and progress of biodegradable zinc alloys and composites for biomedical applications: biomechanical and biocorrosion perspectives, Bioact. Mater. 6 (2021) 836–879, https://doi.org/10.1016/j.bioactmat.2020.09.013.

[33] L. Zhao, P. Yuan, M. Zhang, X. Wang, Y. Qi, T. Wang, B. Cao, C. Cui, Preparation and properties of porous Zn-based scaffolds as biodegradable implants: a review, J. Mater. Sci. 58 (2023) 8275–8316, https://doi.org/10.1007/s10853-023-08561-w.

[34] G.L. Koons, M. Diba, A.G. Mikos, Materials design for bone-tissue engineering, Nat. Rev. Mater. 5 (2020) 584–603, https://doi.org/10.1038/s41578-020-0204-2.

[35] J. Liu, P. Wen, Metal vaporization and its influence during laser powder bed fusion process, Mater. Des. 215 (2022) 110505, https://doi.org/10.1016/j.matdes.2022.110505.

[36] L.C. Capozzi, A. Sivo, E. Bassini, Powder spreading and spreadability in the additive manufacturing of metallic materials: a critical review, J. Mater. Process. Technol. 308 (2022) 117706, https://doi.org/10.1016/j.jmatprotec.2022.117706.

[37] S.C. Altıparmak, V.A. Yardley, Z. Shi, J. Lin, Extrusion-based additive manufacturing technologies: state of the art and future perspectives, J. Manuf. Process. 83 (2022) 607–636, https://doi.org/10.1016/j.jmapro.2022.09.032.

[38] K. Rane, M. Strano, A comprehensive review of extrusion-based additive manufacturing processes for rapid production of metallic and ceramic parts, Adv. Manuf. 7 (2019) 155–173, https://doi.org/10.1007/s40436-019-00253-6.

[39] J. Dong, N. Tümer, M.A. Leeflang, P. Taheri, L.E. Fratila-Apachitei, J.M.C. Mol, A. A. Zadpoor, J. Zhou, Extrusion-based additive manufacturing of Mg-Zn alloy scaffolds, J. Magnes. Alloys 10 (2022) 2491–2509, https://doi.org/10.1016/j.jma.2021.11.018.

[40] J. Dong, Y. Li, P. Lin, M.A. Leeflang, S. van Asperen, K. Yu, N. Tümer, B. Norder, A.A. Zadpoor, J. Zhou, Solvent-cast 3D printing of magnesium scaffolds, Acta Biomater. 114 (2020) 497–514, https://doi.org/10.1016/j.actbio.2020.08.002.

[41] C. Xu, J. Qi, L. Zhang, Q. Liu, L. Ren, Material extrusion additive manufacturing of Ti6Al4V bio-inspired bone implants with tunable Young's modulus, Addit. Manuf. 78 (2023) 103884, https://doi.org/10.1016/j.addma.2023.103884.

[42] G. Zhao, X. Shao, Q. Zhang, Y. Wu, Y. Wang, X. Chen, H. Tian, Y. Liu, Y. Liu, B. Lu, Porous bio-high entropy alloy scaffolds fabricated by direct ink writing, J. Mater. Sci. Technol. 157 (2023) 21–29, https://doi.org/10.1016/j.jmst.2023.02.015.

[43] J. Dong, N. Tümer, N.E. Putra, J. Zhu, Y. Li, M.A. Leeflang, P. Taheri, L.E. Fratila-Apachitei, J.M.C. Mol, A.A. Zadpoor, J. Zhou, Extrusion-based 3D printed magnesium scaffolds with multifunctional MgF2 and MgF2–CaP coatings, Biomater. Sci. 9 (2021) 7159–7182, https://doi.org/10.1039/D1BM01238J.

[44] J. Dong, P. Lin, N.E. Putra, N. Tümer, M.A. Leeflang, Z. Huan, L.E. Fratila-Apachitei, J. Chang, A.A. Zadpoor, J. Zhou, Extrusion-based additive manufacturing of Mg-Zn/bioceramic composite scaffolds, Acta Biomater. 151 (2022) 628–646, https://doi.org/10.1016/j.actbio.2022.08.002.
[45] N.E. Putra, M.A. Leeflang, M. Minneboo, P. Taheri, L.E. Fratila-Apachitei, J.M. C. Mol, J. Zhou, A.A. Zadpoor, Extrusion-based 3D printed biodegradable porous iron, Acta Biomater. 121 (2021) 741–756, https://doi.org/10.1016/j.actbio.2020.11.022.
[46] C. Xu, H. Zhang, S. Yu, W. Wu, L. Zhang, Q. Liu, L. Ren, Direct ink writing of porous Fe scaffolds for bone implants: pore size evolution and effect on degradation and mechanical properties, J. Mater. Res. Technol. 25 (2023) 4901–4912, https://doi.org/10.1016/j.jmrt.2023.06.258.
[47] N.E. Putra, M.A. Leeflang, P. Taheri, L.E. Fratila-Apachitei, J.M.C. Mol, J. Zhou, A.A. Zadpoor, Extrusion-based 3D printing of *ex situ*-alloyed highly biodegradable MRI-friendly porous iron-manganese scaffolds, Acta Biomater. 134 (2021) 774–790, https://doi.org/10.1016/j.actbio.2021.07.042.
[48] N.E. Putra, K.G.N. Borg, P.J. Diaz-Payno, M.A. Leeflang, M. Klimopoulou, P. Taheri, J.M.C. Mol, L.E. Fratila-Apachitei, Z. Huan, J. Chang, J. Zhou, A. A. Zadpoor, Additive manufacturing of bioactive and biodegradable porous iron-akermanite composites for bone regeneration, Acta Biomater. 148 (2022) 355–373, https://doi.org/10.1016/j.actbio.2022.06.009.
[49] N.E. Putra, M.A. Leeflang, M. Klimopoulou, J. Dong, P. Taheri, Z. Huan, L. E. Fratila-Apachitei, J.M.C. Mol, J. Chang, J. Zhou, A.A. Zadpoor, Extrusion-based 3D printing of biodegradable, osteogenic, paramagnetic, and porous FeMn-akermanite bone substitutes, Acta Biomater. 162 (2023) 182–198, https://doi.org/10.1016/j.actbio.2023.03.033.
[50] V. Karageorgiou, D. Kaplan, Porosity of 3D biomaterial scaffolds and osteogenesis, Biomaterials 26 (2005) 5474–5491, https://doi.org/10.1016/j.biomaterials.2005.02.002.
[51] F.J. O'Brien, Biomaterials & scaffolds for tissue engineering, Mater. Today 14 (2011) 88–95, https://doi.org/10.1016/S1369-7021(11)70058-X.
[52] X. Wang, S. Xu, S. Zhou, W. Xu, M. Leary, P. Choong, M. Qian, M. Brandt, Y. M. Xie, Topological design and additive manufacturing of porous metals for bone scaffolds and orthopaedic implants: a review, Biomaterials 83 (2016) 127–141, https://doi.org/10.1016/j.biomaterials.2016.01.012.
[53] T. Ma, B. Zhang, L.M. Lei, Y.C. Wang, Z.M. Song, G.P. Zhang, Tailoring thickness debit for high-temperature fatigue resistance of Inconel 718 superalloy fabricated by laser powder bed fusion, Int. J. Plast. 182 (2024) 104137, https://doi.org/10.1016/j.ijplas.2024.104137.
[54] A. Oyane, H.M. Kim, T. Furuya, T. Kokubo, T. Miyazaki, T. Nakamura, Preparation and assessment of revised simulated body fluids, J. Biomed. Mater. Res. Part A 65A (2003) 188–195, https://doi.org/10.1002/jbm.a.10482.
[55] Corrosion of Metals and Alloys–Removal of Corrosion Products from Corrosion Test Specimens, I. ISO, 8407: 2009 (E), International Standards Organization, Geneva, Switzerland, 2009.
[56] A. Standard, Standard practice for laboratory immersion corrosion testing of metals, Am. Soc. Test. Mater. (2004) G31–G72.
[57] G. ASTM, Standard practice for calculation of corrosion rates and related information from electrochemical measurements, G102–89 (2004).
[58] Z. Zhang, A. Liu, J. Fan, M. Wang, J. Dai, X. Jin, H. Deng, X. Wang, Y. Liang, H. Li, Y. Zhao, P. Wen, Y. Li, A drug-loaded composite coating to improve osteogenic and antibacterial properties of Zn–1Mg porous scaffolds as biodegradable bone implants, Bioact. Mater. 27 (2023) 488–504, https://doi.org/10.1016/j.bioactmat.2023.04.017.
[59] S. Huang, W. Wu, Y. Su, L. Qiao, Y. Yan, Insight into the corrosion behaviour and degradation mechanism of pure zinc in simulated body fluid, Corros. Sci. 178 (2021) 109071, https://doi.org/10.1016/j.corsci.2020.109071.
[60] H. Dong, S. Virtanen, Influence of bovine serum albumin on biodegradation behavior of pure Zn, J. Biomed. Mater. Res. Part B Appl. Biomater. 110 (2022) 185–194, https://doi.org/10.1002/jbm.b.34901.
[61] L. Liu, Y. Meng, C. Dong, Y. Yan, A.A. Volinsky, L.N. Wang, Initial formation of corrosion products on pure zinc in simulated body fluid, J. Mater. Sci. Technol. 34 (2018) 2271–2282, https://doi.org/10.1016/j.jmst.2018.05.005.
[62] Y. Li, P. Pavanram, J. Zhou, K. Lietaert, F.S.L. Bobbert, Y. Kubo, M.A. Leeflang, H. Jahr, A.A. Zadpoor, Additively manufactured functionally graded biodegradable porous zinc, Biomater. Sci. 8 (2020) 2404–2419, https://doi.org/10.1039/C9BM01904A.
[63] I. Cockerill, Y. Su, S. Sinha, Y.X. Qin, Y. Zheng, M.L. Young, D. Zhu, Porous zinc scaffolds for bone tissue engineering applications: a novel additive manufacturing and casting approach, Mater. Sci. Eng. C 110 (2020) 110738, https://doi.org/10.1016/j.msec.2020.110738.
[64] L. Zhao, Z. Zhang, Y. Song, S. Liu, Y. Qi, X. Wang, Q. Wang, C. Cui, Mechanical properties and *in vitro* biodegradation of newly developed porous Zn scaffolds for biomedical applications, Mater. Des. 108 (2016) 136–144, https://doi.org/10.1016/j.matdes.2016.06.080.
[65] Y. Li, P. Pavanram, J. Zhou, K. Lietaert, P. Taheri, W. Li, H. San, M.A. Leeflang, J. M.C. Mol, H. Jahr, A.A. Zadpoor, Additively manufactured biodegradable porous zinc, Acta Biomater. 101 (2020) 609–623, https://doi.org/10.1016/j.actbio.2019.10.034.
[66] Y. Yang, Y. Cheng, S. Peng, L. Xu, C. He, F. Qi, M. Zhao, C. Shuai, Microstructure evolution and texture tailoring of reduced graphene oxide reinforced Zn scaffold, Bioact. Mater. 6 (2021) 1230–1241, https://doi.org/10.1016/j.bioactmat.2020.10.017.
[67] Y. Qin, P. Wen, M. Voshage, Y. Chen, P.G. Schückler, L. Jauer, D. Xia, H. Guo, Y. Zheng, J.H. Schleifenbaum, Additive manufacturing of biodegradable Zn-xWE43 porous scaffolds: formation quality, microstructure and mechanical properties, Mater. Des. 181 (2019) 107937, https://doi.org/10.1016/j.matdes.2019.107937.
[68] M. Voshage, S. Megahed, P.G. Schückler, P. Wen, Y. Qin, L. Jauer, R. Poprawe, J. H. Schleifenbaum, Additive manufacturing of biodegradable Zn-xMg alloys: effect of Mg content on manufacturability, microstructure and mechanical properties, Mater. Today Commun. 32 (2022) 103805, https://doi.org/10.1016/j.mtcomm.2022.103805.
[69] R. Yao, S. Han, Y. Sun, Y. Zhao, R. Shan, L. Liu, X. Yao, R. Hang, Fabrication and characterization of biodegradable Zn scaffold by vacuum heating-press sintering for bone repair, Biomater. Adv. 138 (2022) 212968, https://doi.org/10.1016/j.bioadv.2022.212968.
[70] J. Čapek, J. Pinc, Š. Msallamová, E. Jablonská, P. Veřtát, J. Kubásek, D. Vojtěch, Thermal plasma spraying as a new approach for preparation of Zinc biodegradable scaffolds: a complex material characterization, J. Therm. Spray Technol. 28 (2019) 826–841, https://doi.org/10.1007/s11666-019-00849-1.
[71] A. Cabo Rios, E. Olevsky, E. Hryha, M. Persson, R.K. Bordia, Analytical models for initial and intermediate stages of sintering of additively manufactured stainless steel, Acta Mater. 249 (2023) 118822, https://doi.org/10.1016/j.actamat.2023.118822.
[72] F. Wakai, M. Yoshida, Y. Shinoda, T. Akatsu, Coarsening and grain growth in sintering of two particles of different sizes, Acta Mater. 53 (2005) 1361–1371, https://doi.org/10.1016/j.actamat.2004.11.029.
[73] Y. Zuo, C. Zhao, A. Robador, M. Wickham, S.H. Mannan, Quasi-*in-situ* observation of the grain growth and grain boundary movement in sintered Cu nanoparticle interconnects, Acta Mater. 236 (2022) 118135, https://doi.org/10.1016/j.actamat.2022.118135.
[74] R. German, Sintering theory and practice, in: 1996. https://www.semanticscholar.org/paper/Sintering-theory-and-practice-German/166933206b5f8969a74c310207ba3e8cd6449956 (accessed November 5, 2024).
[75] R. Chaim, On the kinetics of liquid-assisted densification during flash sintering of ceramic nanoparticles, Scr. Mater. 158 (2019) 88–90, https://doi.org/10.1016/j.scriptamat.2018.08.029.
[76] R.M. German, P. Suri, S.J. Park, Liquid phase sintering, J. Mater. Sci. 44 (2009) 1–39.
[77] V. Tikare, J.D. Cawley, Numerical simulation of grain growth in liquid phase sintered materials-I. Model, Acta Mater. 46 (1998) 1333–1342, https://doi.org/10.1016/S1359-6454(97)00269-3.
[78] M. Azar, P. Palmero, M. Lombardi, V. Garnier, L. Montanaro, G. Fantozzi, J. Chevalier, Effect of initial particle packing on the sintering of nanostructured transition alumina, J. Eur. Ceram. Soc. 28 (2008) 1121–1128, https://doi.org/10.1016/j.jeurceramsoc.2007.10.003.
[79] D.J. Delia, W.M. Carty, Limitations on the sintering of graded particle systems, J. Am. Ceram. Soc. 106 (2023) 5689–5697, https://doi.org/10.1111/jace.19259.
[80] B. Paredes-Goyes, D. Jauffres, J.M. Missiaen, C.L. Martin, Grain growth in sintering: a discrete element model on large packings, Acta Mater. 218 (2021) 117182, https://doi.org/10.1016/j.actamat.2021.117182.
[81] A. Mortensen, Kinetics of densification by solution-reprecipitation, Acta Mater. 45 (1997) 749–758, https://doi.org/10.1016/S1359-6454(96)00202-9.
[82] S. Zhou, Y.J. Liang, Y. Zhu, B. Wang, L. Wang, Y. Xue, Ultrashort-time liquid phase sintering of high-performance fine-grain tungsten heavy alloys by laser additive manufacturing, J. Mater. Sci. Technol. 90 (2021) 30–36, https://doi.org/10.1016/j.jmst.2021.02.032.
[83] N. Yang, N. Balasubramani, J. Venezuela, S. Almathami, C. Wen, M. Dargusch, The influence of Ca and Cu additions on the microstructure, mechanical and degradation properties of Zn–Ca–Cu alloys for absorbable wound closure device applications, Bioact. Mater. 6 (2021) 1436–1451, https://doi.org/10.1016/j.bioactmat.2020.10.015.
[84] Y. Zou, X. Chen, B. Chen, Effects of Ca concentration on degradation behavior of Zn-x Ca alloys in Hank's solution, Mater. Lett. 218 (2018) 193–196, https://doi.org/10.1016/j.matlet.2018.02.018.
[85] J. Sun, X. Zhang, Z.Z. Shi, X.X. Gao, H.Y. Li, F.Y. Zhao, J.Q. Wang, L.N. Wang, Development of a high-strength Zn-Mn-Mg alloy for ligament reconstruction fixation, Acta Biomater. 119 (2021) 485–498, https://doi.org/10.1016/j.actbio.2020.10.032.
[86] B. Jia, H. Yang, Y. Han, Z. Zhang, X. Qu, Y. Zhuang, Q. Wu, Y. Zheng, K. Dai, *In vitro and in vivo* studies of Zn-Mn biodegradable metals designed for orthopedic applications, Acta Biomater. 108 (2020) 358–372, https://doi.org/10.1016/j.actbio.2020.03.009.
[87] Y. Su, J. Fu, S. Du, E. Georgas, Y.X. Qin, Y. Zheng, Y. Wang, D. Zhu, Biodegradable Zn–Sr alloys with enhanced mechanical and biocompatibility for biomedical applications, Smart Mater. Med. 3 (2022) 117–127, https://doi.org/10.1016/j.smaim.2021.12.004.
[88] B. Jia, H. Yang, Z. Zhang, X. Qu, X. Jia, Q. Wu, Y. Han, Y. Zheng, K. Dai, Biodegradable Zn–Sr alloy for bone regeneration in rat femoral condyle defect model: *in vitro* and *in vivo* studies, Bioact. Mater. 6 (2021) 1588–1604, https://doi.org/10.1016/j.bioactmat.2020.11.007.
[89] X. Qu, H. Yang, B. Jia, Z. Yu, Y. Zheng, K. Dai, Biodegradable Zn–Cu alloys show antibacterial activity against MRSA bone infection by inhibiting pathogen adhesion and biofilm formation, Acta Biomater. 117 (2020) 400–417, https://doi.org/10.1016/j.actbio.2020.09.041.
[90] M. Wątroba, K. Mech, W. Bednarczyk, J. Kawałko, M. Marciszko-Wiąckowska, M. Marzec, D.E.T. Shepherd, P. Bała, Long-term *in vitro* corrosion behavior of Zn-3Ag and Zn-3Ag-0.5Mg alloys considered for biodegradable implant applications, Mater. Des. 213 (2022) 110289, https://doi.org/10.1016/j.matdes.2021.110289.
[91] Z. Dong, C. Han, G. Liu, J. Zhang, Q. Li, Y. Zhao, H. Wu, Y. Yang, J. Wang, Revealing anisotropic mechanisms in mechanical and degradation properties of

zinc fabricated by laser powder bed fusion additive manufacturing, J. Mater. Sci. Technol. 214 (2025) 87–104, https://doi.org/10.1016/j.jmst.2024.06.045.
[92] F. Xie, X. He, S. Cao, M. Mei, X. Qu, Influence of pore characteristics on microstructure, mechanical properties and corrosion resistance of selective laser sintered porous Ti–Mo alloys for biomedical applications, Electrochim. Acta 105 (2013) 121–129, https://doi.org/10.1016/j.electacta.2013.04.105.
[93] E.E. Abd El Aal, Oxide film formation on zinc in borate solutions under open circuit, Corros. Sci. 50 (2008) 41–46, https://doi.org/10.1016/j.corsci.2007.05.033.
[94] F.E.T. Heakal, A.M. Fekry, A.A. Ghoneim, Corrosion characterization of new tin–silver binary alloys in nitric acid solutions, Corros. Sci. 50 (2008) 1618–1626, https://doi.org/10.1016/j.corsci.2008.02.003.
[95] L.D. Trino, L.F.G. Dias, L.G.S. Albano, E.S. Bronze-Uhle, E.C. Rangel, C.F. O. Graeff, P.N. Lisboa-Filho, Zinc oxide surface functionalization and related effects on corrosion resistance of titanium implants, Ceram. Int. 44 (2018) 4000–4008, https://doi.org/10.1016/j.ceramint.2017.11.195.
[96] C. Gao, M. Yao, S. Li, P. Feng, S. Peng, C. Shuai, Highly biodegradable and bioactive Fe-Pd-bredigite biocomposites prepared by selective laser melting, J. Adv. Res. 20 (2019) 91–104, https://doi.org/10.1016/j.jare.2019.06.001.
[97] Y. Chen, W. Zhang, M.F. Maitz, M. Chen, H. Zhang, J. Mao, Y. Zhao, N. Huang, G. Wan, Comparative corrosion behavior of Zn with Fe and Mg in the course of immersion degradation in phosphate buffered saline, Corros. Sci. 111 (2016) 541–555, https://doi.org/10.1016/j.corsci.2016.05.039.
[98] X. Wang, A. Liu, Z. Zhang, D. Hao, Y. Liang, J. Dai, X. Jin, H. Deng, Y. Zhao, P. Wen, Y. Li, Additively manufactured Zn-2Mg alloy porous scaffolds with customizable biodegradable performance and enhanced osteogenic ability, Adv. Sci. 11 (2024) 2307329, https://doi.org/10.1002/advs.202307329.
[99] R. Hedayati, S. Janbaz, M. Sadighi, M. Mohammadi-Aghdam, A.A. Zadpoor, How does tissue regeneration influence the mechanical behavior of additively manufactured porous biomaterials? J. Mech. Behav. Biomed. Mater. 65 (2017) 831–841, https://doi.org/10.1016/j.jmbbm.2016.10.003.
[100] D. Zhao, C. Han, B. Peng, T. Cheng, J. Fan, L. Yang, L. Chen, Q. Wei, Corrosion fatigue behavior and anti-fatigue mechanisms of an additively manufactured biodegradable zinc-magnesium gyroid scaffold, Acta Biomater. 153 (2022) 614–629, https://doi.org/10.1016/j.actbio.2022.09.047.
[101] Q. Ge, X. Liu, A. Qiao, Y. Mu, Compressive properties and degradable behavior of biodegradable porous zinc fabricated with the protein foaming method, J. Funct. Biomater. 13 (2022) 151, https://doi.org/10.3390/jfb13030151.
[102] Y. Qin, H. Yang, A. Liu, J. Dai, P. Wen, Y. Zheng, Y. Tian, S. Li, X. Wang, Processing optimization, mechanical properties, corrosion behavior and cytocompatibility of additively manufactured Zn-0.7Li biodegradable metals, Acta Biomater. 142 (2022) 388–401, https://doi.org/10.1016/j.actbio.2022.01.049.
[103] International Organization for Standardization, ISO 10993-5: Biological Evaluation of Medical Devices–Part 5: Tests for *In Vitro* Cytotoxicity, ISO, 2009.
[104] X. Tong, X. Shen, Z. Lin, L. Lu, K. Munir, R. Zhou, L. Zhu, Y. Li, J. Ma, C. Wen, J. Lin, *In vitro* and *in vivo* studies of a biodegradable Zn-4Ag-0.1Sc alloy with high strength-elongation product, cytocompatibility, osteogenic differentiation, and anti-infection properties for guided bone-regeneration membrane applications, Chem. Eng. J. 493 (2024) 152763, https://doi.org/10.1016/j.cej.2024.152763.
[105] K. Wang, X. Tong, J. Lin, A. Wei, Y. Li, M. Dargusch, C. Wen, Binary Zn–Ti alloys for orthopedic applications: corrosion and degradation behaviors, friction and wear performance, and cytotoxicity, J. Mater. Sci. Technol. 74 (2021) 216–229, https://doi.org/10.1016/j.jmst.2020.10.031.
[106] H. Kabir, K. Munir, C. Wen, Y. Li, Microstructures, mechanical and corrosion properties of graphene nanoplatelet–reinforced zinc matrix composites for implant applications, Acta Biomater. 157 (2023) 701–719, https://doi.org/10.1016/j.actbio.2022.11.060.
[107] A. Yamamoto, R. Honma, M. Sumita, Cytotoxicity evaluation of 43 metal salts using murine fibroblasts and osteoblastic cells, J. Biomed. Mater. Res. 39 (1998) 331–340, https://doi.org/10.1002/(SICI)1097-4636(199802)39:2<331::AIDJBM22>3.0.CO;2-E.
[108] D. Liang, M. Yang, B. Guo, J. Cao, L. Yang, X. Guo, Zinc upregulates the expression of osteoprotegerin in mouse osteoblasts MC3T3-E1 through PKC/MAPK pathways, Biol. Trace Elem. Res. 146 (2012) 340–348, https://doi.org/10.1007/s12011-011-9254-z.
[109] L.S. Wan, Z.K. Xu, X.J. Huang, Z.G. Wang, J.L. Wang, Copolymerization of acrylonitrile with *N*-vinyl-2-pyrrolidone to improve the hemocompatibility of polyacrylonitrile, Polymer 46 (2005) 7715–7723, https://doi.org/10.1016/j.polymer.2005.05.147.
[110] G. Chen, P. Cao, G. Wen, N. Edmonds, Debinding behaviour of a water soluble PEG/PMMA binder for Ti metal injection moulding, Mater. Chem. Phys. 139 (2013) 557–565, https://doi.org/10.1016/j.matchemphys.2013.01.057.
[111] Q. Liu, A. Li, S. Liu, Q. Fu, Y. Xu, J. Dai, P. Li, S. Xu, Cytotoxicity of biodegradable zinc and its alloys: a systematic review, J. Funct. Biomater. 14 (2023) 206, https://doi.org/10.3390/jfb14040206.